# CHALMERS

Wading – Evaluation of SPH-based simulations versus traditional Finite Volume CFD

Master's thesis in Applied Mechanics

JOHAN IDOFFSSON

MASTER'S THESIS IN APPLIED MECHANICS

Wading – Evaluation of SPH-based simulations versus traditional Finite Volume CFD

JOHAN IDOFFSSON

Wading – Evaluation of SPH-based simulations versus traditional Finite Volume CFD
JOHAN IDOFFSSON

Cover:
Rendering of SPH simulation showing a XC60 wading at a depth of 400 mm and a speed of 6 km/h

Wading – Evaluation of SPH-based simulations versus traditional Finite Volume CFD
Master's thesis in Applied Mechanics
JOHAN IDOFFSSON
Department of Mechanics and Maritime Sciences
Division of Fluid Mechanics
Chalmers University of Technology

Abstract

Going through deep water is a driving condition connected with many potential problems for ground transportation vehicles. It exerts additional forces on the external parts of the vehicle not present during normal driving. In combustion vehicles, it may hinder the required constant supply of air to the engine, or it might even flood. Simulations to study this driving condition are normally conducted at Volvo Car Corporation (VCC) using a traditional Finite Volume Method (FVM) namely, Volume Of Fluid (VOF), either conducted in StarCCM+ or OpenFOAM. These simulations are performed in an Eulerian framework requiring a computational mesh. This requirement aggravates the replication of real life conditions. A new alternative to the current method has been developed, Smooth Particle Hydrodynamics (SPH). SPH is a particle method conducted solely in a Lagrangian framework removing the need of a computational volume mesh.

The SPH method has many advantages over the one used today, most importantly having the potential of reducing simulation times drastically. The purpose of this master thesis is to investigate the potential use of a SPH solver as a substitute or complement to VOF in wading simulations at VCC. Due to the versatility of the method, a setup that mimics real world phenomena and kinematics is sought. The methodology includes methods to do visual assessments together with force measurements, water ingress, as well as performance in terms of computational cost.

SPH has proven to be a reliable framework that is both capable of predicting phenomena in a frame of reference both agreeing with the existing FVM and real-world conditions. In terms of computational time, great reductions can be achieved through an adaptive domain size. The developed method is not complete, and there are still room for future improvement. At this date, SPH has proven to be a competitive alternative to VOF.

Keywords: SPH, VOF, Wading, FVM, Evaluation, PreonLab, Simulation, Physical testing

Preface

This report is the result of a Master's thesis project at the Department of Mechanics and Maritime Sciences at Chalmers University of Technology between January and June 2019. The project was carried out at Volvo Car Corporation in Gothenburg with the purpose of investigating the use of a SPH solver to study vehicle wading and compare the method with an existing one using the VOF method. The new method was proving to perform well and many advantages over the existing method was found. With the acquired knowledge through this work a new method should be possible to implement in the design process in order to build more reliable vehicles.

Acknowledgements

Johan Idoffsson
Göteborg, June 2019

NOMENCLATURE

CAC   Charge Air Cooler
CBF   Continuum Boundary Force
CFD   Computational Fluid Dynamics
CFL   Courant-Freidrish-Lewy number
CG   Center of Gravity
DNS   Direct Numerical Simulation
EU   European Union
FVM   Finite Volume Method
HPG   Hällered Proving Ground
PF   Pairwise Force
PID   Property Identifier
SPH   Smoothed Particle Hydrodynamics
STL   Stereolithography
VCC   Volvo Car Corporation
VOF   Volume Of Fluids

α, β Artificial viscosity constant
$\bar{\mu}$ Averaged dynamic viscosity
$\bar{\rho}$ Averaged density
δ Delta dirac function
γ Volume fraction
$\hat{\mathbf{n}}$ Surface normal vector
ν, μ Viscosity, kinematic and dynamic
Π Artificial viscosity
ρ Density
σ Surface tension constant
A Arbitrary scalar or vector
c Speed of sound in water
F Force lift/drag
Fr Froude number
g Gravity constant
h Supporting range
h_m Hydraulic depth
h_{CG} Height of center of gravity
k Surface curvature
m Mass
p Pressure

q	Normalizied kernel distance
t	Time
V	Volume
W	Kernel function
WB	Wheel base
WB_F	Distance from front axle to the center of mass
WB_R	Distance from rear axle to the center of mass
We	Weber number
$\mathbf{f}$	Body force
$\mathbf{F}_\sigma$	Surface tension
$\mathbf{r}$	Position vector
$\mathbf{T}$	Stress tensor
$\mathbf{v}$	Velocity

Contents

List of Figures

List of Tables

1 Introduction

Numerical simulations play a big role in the development of new vehicles. The tools available alleviate the need of physical testing, which might be expensive and limited in terms of what that can be measured. It can also reduce the time spent in development as simulations can be conducted much earlier in the design phases. Wading is a particularly difficult driving condition to investigate where the need of accurate simulation models are interesting. In the following chapter the background to this thesis is described together with the purpose, some limitations and a thesis outline.

1.1 Background

New target levels in terms of CO_2 emissions have been set by the European Union (EU) to have a 15% reduction from 2025 on and a 37.5% reduction from 2030 on [1], relative the values of today. In 2016 the road transport sector contributed to nearly 21% of the EU's total emission of CO_2. Light duty vehicles and vans were responsible for around 15% of the total 21%. The new target levels are one of many action to reduce the total emission of CO_2 and limit the global warming to levels set by the Paris agreement of no more than 2 degrees Celsius [2].

By 2025 VCC aims at having a 50% annual sale rate of fully electric vehicles [3]. Moreover, there is an ambition of reducing the time of development in new projects. The former follows the new directives to restrict the emissions while the latter makes for a more lean and efficient development process, where costs can be reduced. This sets high demand on time management and shrinks the time span in which design changes can be made. Relying on physical testing, prototype vehicles have to be constructed, which usually happens late in the projects. By that time, design changes are more costly and the freedom of design is compromised. Using the aids of simulations, tests can be performed earlier in the projects while still having more flexibility in alterations.

Going through deep water, referred to in this report as wading, is a driving condition connected with many potential problems for ground transportation vehicles. It exerts additional forces on the external parts of the vehicle not present during normal driving. In combustion vehicles, it may hinder the required constant supply of air to the engine, or it might even flood. Regarding electrified vehicles, there are several dangers connected to the batteries. Electrical parts, e.g. batteries, are often positioned near the floor to lower the centre of gravity. This makes these parts especially sensitive to high water levels. In figure 1.1 two driving scenarios are presented going through water with a depth of 400 mm. In (a), using a lower vehicle speed, a calm behaviour of the water is achieved while the opposite is seen for higher speed, as in (b).

(a) *400 mm 6 km/h*   (b) *400 mm 12 km/h*

Figure 1.1: *Vehicle wading at two different speeds. The water depth is 400 mm*

The tools which can be used to assess the behaviour of wading tests are limited and relies mostly on visual means. The complexity of the nature of the flow field cannot be visualised, and the root cause of design faults may never be found. By adopting numerical simulations the user gets full control of the events, as long as one is aware of the limitations and modelling assumptions. Simulations to study this driving condition are normally done at Volvo Cars using a traditional FVM namely, VOF, either conducted in StarCCM+ or OpenFOAM. These simulations are performed in an Eulerian framework requiring a computational mesh. This requirement aggravates replicating real life conditions. If a geometry change is to be conducted, e.g. mimic the behaviour of a rotating wheel, a new computational mesh has to be created at every timestep. A change of reference is also assumed, prescribing a velocity to the incoming water, while having the car stationary. Due to these circumstances, simulations of this type are computationally heavy and results cannot be kept up with the sheer number of needed evaluations. The reliability of the results are also questionable.

A new alternative to the current method has been developed, SPH. This is a particle method conducted solely

in a Lagrangian framework removing the need of a computational volume mesh. The method was originally developed to simulate phenomena in astrophysics [4] but the field of use has now been broadened including multiphase flows. This method has many advantages over the existing one used, with the potential of reducing simulation times drastically. Bodies in the domain can be translated and rotated at a low computational cost by changing the boundary conditions. These advantages may come at the cost of a reduced accuracy in the simulation. In this study the use of SPH is evaluated using the software PreonLab (ver. 3.1.2 and 3.3.0) developed by Fifty2 Technology GmbH.

Despite the fact that this evaluation and method development is not done explicitly on electric vehicles in this thesis, a generic model is developed which allows the use of any vehicle type. The parameters adopted in the study suits well for the used vehicle model and supports the comparisons made, both in terms of the different modelling frameworks and simulations versus reality.

1.2   Purpose

The purpose of this master thesis is to investigate the potential use of a SPH solver as a substitute or complement to VOF in wading simulations at VCC. Due to the versatility of the method a setup that mimics real world phenomena and kinematics are sought. The study is divided into three major areas as presented below:

SPH vs VOF
A comparative study is conducted to evaluate how SPH and VOF compares using an identical simulation environment.

Features of SPH
The SPH solver is investigated in order to look at different modelling features and how the computational domain affect the simulation results.

SPH vs Physical testing
A simulation setup is constructed with the purpose of replicating real world conditions. The model is compared to physical tests, where the use of visual aids is used together with sensor data.

1.3   Limitations

Some limitations are given in the project, defined as follows:

This thesis work is conducted by one student over a time frame of 20 weeks, equal to 30 ECTS.

One vehicle model, adopting two configurations, is used to conduct all simulations in this study, the latest version of the XC60. The two configurations are based on prototypes and hence not in production. Some features differ from similar production cars meaning that the results presented are not valid for vehicles available to costumers.

One wading depth, 400 mm, is used throughout the thesis. The used wading depth is greater than the maximum depth set in the specifications of the vehicle. The reason for using this depth is to be able to detect certain phenomena and larger differences between the individual tests.

1.4   Outline

This thesis is divided into six chapter. This introduction is followed by a chapter describing the underlying theory of the respective methods used. As the first method, VOF, is well established, less focus is devoted to that method here. SPH, on the other hand, is dealt with more thoroughly due to its novelty. Afterwards, the methodology is described, having the same division on the level of description as in the theory chapter. In the next chapter all results are presented, keeping the level of discussion low. This is however dealt with in more detail in the second to last chapter devoted solely to this. Finally, a conclusion is presented summing up the work and thesis as a whole.

2 Theory

In the following chapter the underlying theory for the respective methods and concepts are presented. Initially, a section is devoted to VOF and its underlying theory. Afterwards, the background and fundamentals of SPH are presented. Different papers have been used to create a comprehensive picture of the latter method and its applications, while the prior is presented more shortly. The chapter is ending with some features of PreonLab and finally two useful non-dimensional numbers.

2.1 Multiphase modelling

Multiphase flows are present in a wide range of applications. It can be the case of a dispersed phase in a fluid, e.g. particles in water, or two immiscible fluids interacting [5]. There are a great number of methods, employing different approaches and assumptions, to describe the physics of such flows and there is no definite answer to which method is best suited in a particular case. What makes these kinds of flow most difficult to deal with is the complexity in the modelling, and what to account for. Which method is chosen will determine the information that is stored within the system and what is lost. One phase might change into another and the physics can take place on many different scales, time- and lengthwise. Two major frameworks can be employed to describe the physics and how the flow is tracked, Eulerian and Lagrangian methods. In the case of the former method, the flow is described using a predefined fix coordinate system, from which all calculations are made, creating fields. The most common method within this framework, is the FVM, in which a grid is used to discretize the domain of interest. In the latter framework all entities in the flow are followed, using a coordinate system moving with the flow. In a pure Lagrangian framework there is no need to discretize the domain. The communication between the two reference frames can be described as that the Lagrangian property associated with fluid particles at a point is the same as the Eulerian property at the same point [6]. The two frameworks can be used separately or combined, to describe different phases in the same flow. In the case of immiscible fluids, these are often described as free surface flows, including a sharp interface between them. These types of flow are of most interest in this work and described in more detail below.

2.1.1 Free surface modelling

Free surface modelling can be approached both using Eulerian and Lagrangian methods. In the case of a grid based Eulerian frameworks the methods used can be categorised as volume and surface methods. Both of these are described as Direct Numerical Simulations (DNS) of multiphase flows. When employing volume methods, the interface is tracked implicitly, implying that the interface is not taken as a boundary condition and rather as a part of the solution. By capturing the interface, the resolution of the solution will be dependent on the discretization of the domain. Breakups and small volumes of fluid, e.g. due to splashing, is not captured if the grid is too coarse. On the other hand, using surface methods, the interface is tracked explicitly and recreated. For this case topology changes, due to breakup and coalescence is done manually and can be performed on a sub grid level. Both methods can deal with high levels of topology complexity. VOF is an implicit Eulerian method which will be described in more detail below.

When employing a Lagrangian method there is no need divide the domain, using a grid. Instead, the fluids themselves are discretized. Like for Eulerian methods, complex boundary dynamics are easily handles using this method. No reconstruction of interfaces are needed due to the nature of the modelling. One pure Lagrangian method is SPH, which is the main method of focus in this work.

2.2 Wading

Wading is a driving condition associated with driving through deep water, up to depths of around 500 mm. This situation can typically be described by two separate regions of fluids, water and air, separated by a sharp interface. Due to the vehicle movement, a bow wave, in front of the vehicle will occur, elevating the waterline. By moving in the lengthwise direction of the vehicle the waterline level will gradually decrease [7]. The wave propagation and free surface behaviour will be dependent on, except for the initial water depth, the vehicle speed, which is in the range of around $10\,\mathrm{km/h}$.

2.3 VOF

VOF is a DNS method for calculating multiphase flows suitable for immiscible fluids. The method is implicit in the sense that the interface between two, or more phases, is a part of the solution, and not reconstructed. In the following section the governing equations are presented and the terms are described. Here, the equations are given assuming a two phase situation.

In this model the individual phases are represented using only one set of momentum equations, where the density and stress tensor are determined using weighted contributions of the respective phases. The weighting is performed using a color function. This color function can be chosen as the volume fraction γ, which means it will be in the range of zero to one. A volume fraction equal to zero indicates that the cell in question is only occupied by phase 1. If the volume fraction is equal to one it is only occupied by phase 2. If a value between zero and one is taken the cell is occupied by both phases, indicating an interface. The momentum equations are solved together with the continuity equation, which is given on the following form [8].

$$\nabla \cdot \mathbf{v} = 0 \tag{2.1}$$

assuming incompressible flow. The momentum equations, assuming the same condition, takes the form of

$$\nabla \cdot (\mathbf{v}\mathbf{v}) = \frac{1}{\rho}\nabla \cdot \mathbf{T} + \mathbf{f} + \mathbf{F}_\sigma. \tag{2.2}$$

The density, ρ, and the stress tensor, $\mathbf{T}$, are altered using the above mentioned weighting function, to account for phase transitions. $\mathbf{f}$ is a body force while $\mathbf{F}_\sigma$ is a surface tension force contribution, acting as a body force too, only present close to interfaces.

$$\rho = \gamma\rho_1 + (1-\gamma)\rho_2, \quad \mathbf{T} = \gamma\mathbf{T}_1 + (1-\gamma)\mathbf{T}_2 \tag{2.3}$$

In order to track the interface the volume fraction itself needs to be solved for using the following convection equation.

$$\frac{\partial \gamma}{\partial t} + \mathbf{v} \cdot \nabla\gamma = 0 \tag{2.4}$$

In order to maintain a sharp interface, stretching no more than one cell in the domain, a non-diffusive discretization scheme is preferable. The surface tension is applied as a body force acting only close to interfaces, controlled by a delta function, δ. This sets high requirements on the mesh resolution and the diffusivity of the discretization scheme of the convective volume fraction equation to maintain a sharp and physically sound force. The force can be described as follows:

$$\mathbf{F}_\sigma = \sigma k \hat{\mathbf{n}}\delta. \tag{2.5}$$

By utilising the characteristics of the color function, the delta function can be constructed to apply the surface tension force only at the interface. The surface normal, $\hat{\mathbf{n}}$, and curvature, k, also need to be calculated. This is done, once again, adopting the color function. The delta function, curvature and surface normal can be described as:

$$\delta = |\mathbf{n}|, \quad k = -\nabla \cdot \hat{\mathbf{n}}, \quad \hat{\mathbf{n}} = \frac{\nabla\gamma}{|\nabla\gamma|}. \tag{2.6}$$

2.4 SPH

SPH was initially formulated in the field of astrophysics to simulate nonaxisymmetric phenomena [4]. Due to its stability and predictability it was later extended to model fluid flows. It is a purely Lagrangian method where the fluid volume is represented by a set of particles. The nonlinearities present in the inertial term, in the momentum equations, and the boundary condition at fluid-fluid or fluid-solid interfaces are easily handled using SPH [9]. Differential operators are approximated with integrals, and integrals are approximated with Riemann sums. Many different formulation of the including terms has been developed. In this report multiple papers have been used to concatenate the governing equations. Due to the low level of coupling between the two fluids in the regions present in this thesis, the air is not taken into account in the presented formulation. This approach has also been used in this work as PreonLab uses this very way of describing the flow. In the following sections, the SPH formulation and assumptions are presented.
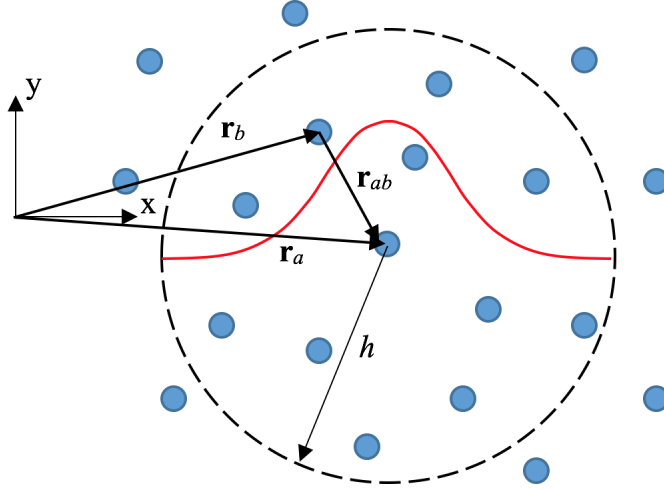
Figure 2.1: *The kernel function acting on adjacent particles to particle a. The supporting range is represented by the black dashed circle surrounding the volume in which the summations are done.*

2.4.1 Fundamentals of SPH

The key to SPH is the assumption that all scalar or tensor quantities, $A(\mathbf{r})$, can be rewritten as integral interpolants over the entire space defined by [4]

$$A(\mathbf{r}) = \int A(\mathbf{r}')W(\mathbf{r} - \mathbf{r}', h)\mathbf{dr}' \tag{2.7}$$

where W is a smoothing kernel, which is a function of the euclidean norm $\|\mathbf{r} - \mathbf{r}'\|$. This function has two important properties,

$$\int W(\mathbf{r} - \mathbf{r}', h)\mathbf{dr}' = 1 \tag{2.8}$$

implying that the kernel is normalized, and tends to a Dirac delta function as $h \rightarrow 0$, written as,

$$\lim_{h \rightarrow 0} W(\mathbf{r} - \mathbf{r}', h) = \delta(\mathbf{r} - \mathbf{r}') \tag{2.9}$$

where h is defined as the supporting range, in which the interpolation is performed and W is non-zero. This supporting range is introduced to reduce the computational cost. A representation of the kernel function is presented in figure 2.1. This interpolant is later approximated with a summation. The summation is written on the following form

$$A_S(\mathbf{r}) = \sum_b m_b \frac{A_b}{\rho_b} W(\mathbf{r} - \mathbf{r}_b, h) \tag{2.10}$$

where A_S, m_b and ρ_b are the summation approximation, mass and density of adjacent particle b relative particle a, respectively. The summation is done over all particles within the supporting range h. Similarly, the gradient of A is defined as

$$\nabla A_S(\mathbf{r}) = \sum_b m_b \frac{A_b}{\rho_b} \nabla W(\mathbf{r} - \mathbf{r}_b, h) \tag{2.11}$$

Since the kernel function is defined by functions, it can easily be differentiated. This is one powerful feature of the SPH formulation. An issue that rises near free surface is the truncation of the Riemann sum due to a deficit of adjacent particles. This will introduce a nonphysical velocity field close to the surface. This in turn will result in incorrect velocity gradients and turbulent viscosity.

2.4.2 Lagrangian formulation

In order to derive the governing equations of the SPH formulation the Navier-Stokes equations are written on Lagrangian form. The equations are written here on incompressible form and can be expressed as [10]

$$\frac{d\mathbf{v}_a}{dt} = -\frac{1}{\rho_a}\nabla p_a + \nu_a\nabla^2\mathbf{v}_a + \nabla\Phi_a + \mathbf{f}_a \tag{2.12}$$

where the subscript a indicates that all terms are connected to one particular particle. On the left hand side the time derivative of the particle velocity is given. On the right hand side the pressure gradient, viscous diffusion, surface tension and a body force are given. The first three terms on the right hand side are now presented separately and expressed using the SPH formulations. Different papers have been used to give a complete picture of the formulation and the diversity of developed methods.

2.4.3 Pressure term

The pressure term, given in equation 2.13, is presented on a symmetric form allowing for perfect linear and angular momentum conservation [4]. Here, the kernel W has been written on a shorter form where, $W_{ab} = W(\mathbf{r}_a - \mathbf{r}_b, h)$. This formulation will be used from this point on. If the equation is not written on a symmetric form isolated pairs of particles with different pressures would bootstrap themselves to infinity [4]. This formulation does not however ensure that the pressure gradient equals zero when two adjacent particles have the same pressure.

$$-\frac{1}{\rho_a}\nabla p_a = -\sum_b m_b\left(\frac{p_a}{\rho_a^2} + \frac{p_b}{\rho_b^2}\right)\nabla W_{ab} \tag{2.13}$$

2.4.4 Viscous diffusion term

The viscous diffusion term is estimated employing Morris et al. [11] presented in equation 2.14. The summation is initially written on a symmetric form, but as all particles have the same dynamic viscosity, the formulation is somewhat simplified. The formulation conserves linear momentum exactly, while the angular momentum is only approximately conserved [11].

$$\nu_a\nabla^2\mathbf{v}_a = \sum_b \frac{m_b(\mu_a + \mu_b)\mathbf{v}_{ab}}{\rho_a\rho_b}\left(\frac{1}{\|\mathbf{r}_{ab}\|}\frac{\partial W_{ab}}{\partial r_a}\right) = \{\mu_a = \mu_b, \rho_a = \rho_b\} = \sum_b\left(\frac{2\nu_b V_b}{\|\mathbf{r}_{ab}\|}\frac{\partial W_{ab}}{\partial r_a}\right)\mathbf{v}_{ab} \tag{2.14}$$

In order to yield an additional stabilization when modelling higher Reynolds numbers an artificial viscosity can be employed on the form [4]

$$-\sum_b m_b\Pi_{ab}\nabla W_{ab} \tag{2.15}$$

where

$$\Pi_{ab} = \begin{cases} \dfrac{-\alpha c\tilde{\mu}_{ab} + \beta\tilde{\mu}_{ab}^2}{\bar{\rho}_{ab}}, & \text{if } \mathbf{v}_{ab}\cdot\mathbf{r}_{ab} < 0; \\ 0, & \text{otherwise} \end{cases} \tag{2.16}$$

$$\tilde{\mu}_{ab} = \frac{h\mathbf{v}_{ab}\cdot\mathbf{r}_{ab}}{\mathbf{r}_{ab}^2 + 0.01h^2} \tag{2.17}$$

This implies that particles moving towards each other will feel an additional repelling force reducing their relative velocity. If they, on the other hand are moving away from each other, no additional influence of this viscous diffusion term will be applied. This is the SPH equivalent of $\nabla\cdot\mathbf{v} > 0$.

2.4.5 Surface tension term

There are different methods that can be employed for imposing the Young-Laplace boundary condition at fluid-fluid interfaces and the Young condition at fluid-solid interfaces. The most common methods are the Continuum Boundary Force (CBF) and the Pairwise Force (PF). In both models, the boundary conditions are replaced with forces with non-zero net contributions only near the boundaries. In CBF models the surface

tension is directly computed from the Young-Laplace and Young conditions and applied over a finite volume near the interface. The interface is tracked using for instance a condition on the density, such as $\rho < 0.99\rho_0$ [12], or on the kernel function, as $\sum_b W(\mathbf{r}_{ab}, h) < 0.97$ [13]. The interface normal and curvature are needed to be calculated using the near surface particles. Due to this, a surface normal recreation is more difficult for coarser particle flows. As the CBF only is applied on a finite layer on the surface it is also difficult to ensure conservation of momentum.

The PF model assumes a pairwise molecular like force [9]. The model computes a force between all pairs of particles within a kernel, based on their relative distance. As the model is applied to all particles it ensures perfect momentum conservation and is invariant with respect to the particle resolution.

One version of the PF surface tension model is presented in equation 2.18 [9]. The model takes both the cohesion property for particle-particle interaction and adhesion property for particle-solid interaction into account. The ratio of the cohesion and adhesion properties determine the wetting properties on surfaces. The surface tension is calculated as:

$$\nabla\Phi_a = -\sum_b \sigma w^c(q)\frac{\mathbf{r}_{ab}}{h^2}, \quad q = \frac{\mathbf{r}_{ab}}{h} \tag{2.18}$$

where σ is the cohesion and adhesion properties of adjacent particles. The kernel function $w_c(q)$ is defined as:

$$w_c(q) = \frac{9}{64\pi}\begin{cases} 2(2-q)^3 q^3 - 1 & 0 \leq q \leq 1, \\ (2-q)^3 q^3 & 1 < q < 2 \\ 0 & q \geq 2 \end{cases} \tag{2.19}$$

Three different regions can be identified. This is illustrated in figure 2.2 where the model imposes both an attractive and repelling force depending on particle-particle distance. At distances greater than $2q$ the force has no contribution.
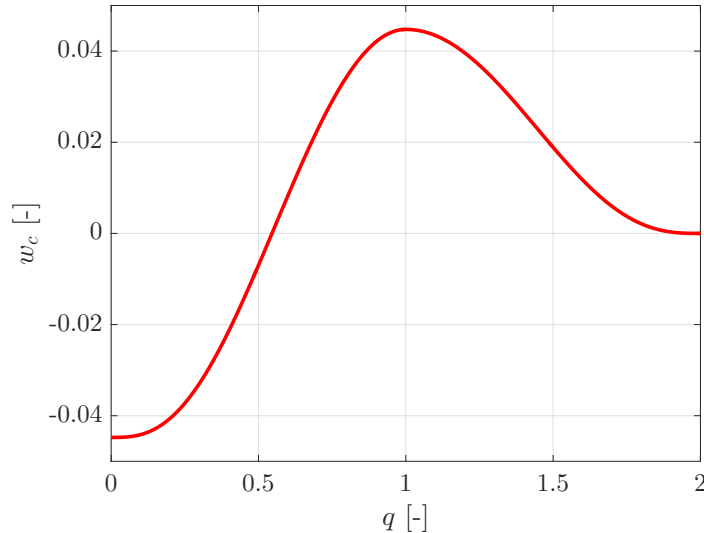

Figure 2.2: *The kernel function used to calculate the surface tension particle-particle/particle-boundary interaction. Particles closer than $0.5q$ experience a repelling force while particles at a longer distance experience an attracting force. Particles at a distance greater than $2q$ has no influence on the surface tension, reducing the computational cost.*

(a) *Initial grille geometry*   (b) *Grille geometry represented by boundary particles*
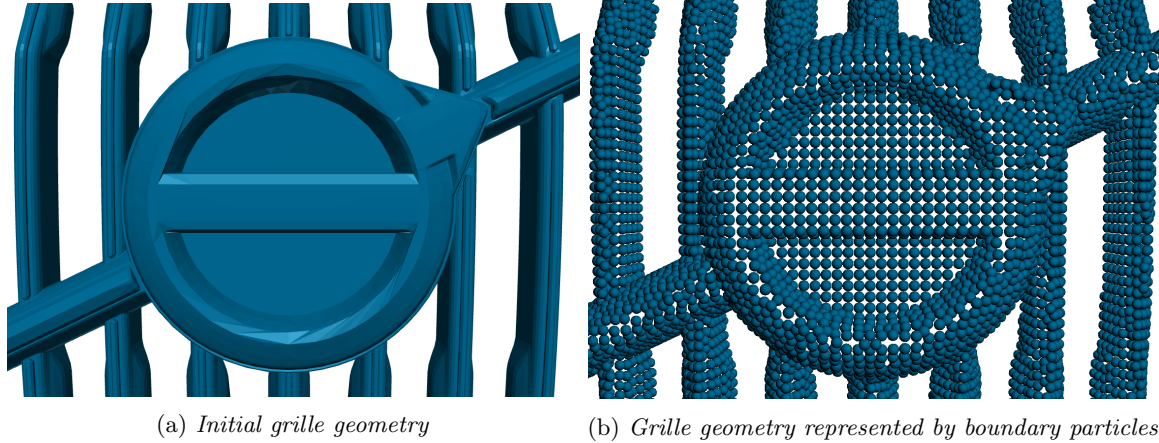
Figure 2.3: *The difference in the boundary representation between the input geometry and the boundary represented by particles. In the right image a particle spacing of 5 mm has been used. Both images have been created in PreonLab*

2.4.6 SPH formulation

By collecting and substituting all contributing terms, the momentum equation in the SPH formulation gets the following form.

$$\frac{\mathrm{d}\mathbf{v}_a}{\mathrm{d}t} = -\sum_b m_b \left(\frac{p_a}{\rho_a^2} + \frac{p_b}{\rho_b^2} + \Pi_{ab} \right) \nabla W_{ab} + \sum_b \left(\frac{2\nu_b V_b}{\|\mathbf{r}_{ab}\|} \frac{\partial W_{ab}}{\partial r_a} \right) \mathbf{v}_{ab} - \sum_b \sigma w^c(q) \frac{\mathbf{r}_{ab}}{h^2} + \mathbf{f}_a \tag{2.20}$$

The last term, left untouched, has no need to be approximated, using a summation. With this complete form, the equations can be solve for a set particles. How this is done will be left out of this report. The continuity equation can also be written on multiple forms. One approach [4] uses the following formulation

$$\frac{\mathrm{d}\rho_a}{\mathrm{d}t} = \sum_b m_b \mathbf{v}_{ab} \cdot \nabla W_{ab} \tag{2.21}$$

In this approach the density of every particle is set before the simulation is started and changes in the local density will only vary when particles move relative to each other.

2.4.7 Boundary representation

Rigid boundaries have been represented using different methods, including both ghost particles [14] and layers of fixed boundary force particles [15]. The former method employs imaginary particles mirrored through the boundary, where the velocity is set to match the boundary condition of interest. This method is suitable in the case of flat boundaries, where it is evident how the particles should be reflected. Problems arise in the case of high surface curvatures which can introduce artificially large or small fluid densities [14]. This method does however provide a smoother behaviour of the particles near the boundaries. This is of extra interest when pressure fields along the boundary are sought. The latter method employs a set of fixed fluid particles acting on the fluid. This method works better for large boundary curvatures. Unlike the first method, this one introduces a truncation error in the summation due to the deficit of particles inside of the boundary for near wall calculations. Oscillations in the pressure field can occur due to the fact that the force acting on the adjacent particle only depend on their distance to the walls [16]. A small change in the distance to the wall will have a big influence in the repellent force acting on the fluid particle. Both methods have problems in their respective formulations and are suitable for different applications. An example of how a boundary particle representation may look like is presented in figure 2.3.

2.4.8 Particle spacing

The particle spacing describes the size of the particles in the formulation. A smaller particle size corresponds to a higher resolution of the flow. The number of particles increases cubically with decreasing particle spacing.

By reducing the particle size to half of its original size, the number of particles in the domain will increase by eight times. The particles spacing can either be fixed or variable in space. For the former case, if the flow needs to be resolved at a higher level in one part of the domain due to small geometries and voids, less important areas still needs to be resolved at the same higher resolution. In the case of a variable resolution, various methods have been developed. Ulrich et al. [17] adopt a method using an Eulerian approach, known as an Eulerian variable-resolution technique, where the particle properties are altered over transitional regions in the domain. Source terms are added to both the continuity and momentum equations to account for the transitions. Problems related to mass and momentum conservation can be introduced for this latter approach. On the other hand, this approach can significantly reduce the computational time of the simulation.

2.5 Calculation of surface forces

Surface forces are calculated by integrating projected wall shear and normal stresses over the surface of interest, as is show in equation 2.22. The subscript α represents the two directions of interest in this report, namely, x and z, where x is defined as the negative direction of travel and z as the vertical direction.

$$F_\alpha = \int_A (-p_s + \tau_w)\hat{\mathbf{n}}_\alpha \mathrm{dA} \tag{2.22}$$

2.6 PreonLab

PreonLab is a software, developed by Fifty2 Technology GmbH, employing the SPH formulation to solve fluid flows. It is suitable for free surface flows, adopting a single-phase free surface approach. In this thesis, this phase will be water. The accounted phase can be interpreted to be simulated in a vacuum, with no coupling to its surroundings apart from rigid boundaries in the computational domain. In order to replicate the conditions of having a second phase, for instance air, a predefined flow field can be imported, either as a constant or space varying, to introduce a coupling between the two phases, acting as interpolated point sources. This will not be done in this work. The terms in the governing equations are approximated as was described under section 2.4.6. Some features, specific to the solver, are presented below.

2.6.1 Modelling time step

While conducting the numerical integration of the governing equations, one needs to make sure that the time step is satisfactory in order to receive physically sound results and a stable solution. A condition often employed to determine the size of the time step is the Courant-Friedrish-Lewy (CFL) number. The number describes the ratio between distance a particle travels over one time step and the particle spacing. A CFL number no larger than 1 should be strived for [18] in order to achieve physical results in PreonLab. The CFL number is written as:

$$\mathrm{CFL} = \frac{\Delta t \|\mathbf{v}_a\|}{h} \tag{2.23}$$

In Preonlab one has the option to either set a defined time step or an adaptive. In the latter case the solver will automatically update the time step according to the highest particle velocity in the domain using a fix CFL number. A condition used to delete particles with too high velocity can also be applied in order to hinder excessively small time steps.

2.6.2 Particle domain types in PreonLab

The behaviour of the particles in the simulation are decided by the type of bounding box they are present in. In order for the particles to behave according to the governing equations, they must be contained in a computational box. If no computational box is present, the whole domain will be considered as this domain type. If one is present and a particle moves outside of it, its behaviour is determined by predefined conditions. These conditions are applied on the particles velocity. It could be that the particle is given a constant velocity in a certain direction or kept stationary. To remove particles, a deletion domain can be introduced. Particles entering this space will be deleted instantaneously.

(a) *Gap representation*   (b) *No gap representation*
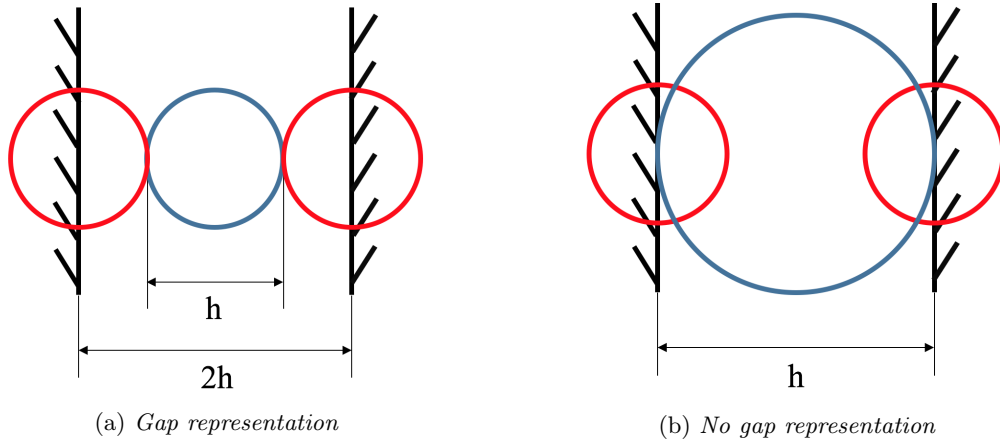
Figure 2.4: *The difference between a gap or no gap boundary representation. In the left image, the boundary particles are sampled with a diameter equal to the fluid particle spacing. In the right image the boundary particles are sampled with half the particle spacing. Boundary particles are represented by red circles while fluid particles are blue. Note that the scales are not equal between the left and right image.*

2.6.3 Boundary handling

Two alternative methods can be employed to describe boundaries in PreonLab, one coarser which is less computationally heavy and one finer which is more demanding. In the former case all boundaries are sampled and represented by particles with the same spacing as the fluid particles in the domain. This will enforce a physical gap between particles adjacent to the walls and the walls themselves. Gaps more narrow than $2h$, where h is the particle sampling, will not be resolved. A remedy to this problem is to sample boundary particles with half the diameter. As a consequence, boundary particles need to have a modified kernel with half the supporting range, $h/2$. This technique can be used as an alternative to refining all particles in the domain, given that the flow is sufficiently resolved. The two different representation can be seen in figure 2.4.

In terms of boundary particle pressure calculations there are two methods too. One method is to let boundary particles be treated the same way as fluid particles and hence pressures are calculated explicitly taking part in the computation. To reduce the computational time fluid pressures of adjacent boundary particles can be mirrored onto surfaces. The latter method is less accurate.

2.6.4 Car Suspension Model

A simplified car suspension model can be implemented in PreonLab in order to account for buoyancy effects. By integrating the external forces on the car a displacement of the car body can be carried out. These forces are applied at the front and rear wheel axles and introduces additional moments around the center of gravity of the vehicle. The model allows for the additional degrees of freedom related to translation of the sprung mass of the vehicle in the direction normal to ground and rotation around the y-axis at the center of gravity. The vehicle is modelled as a mechanical system employing a spring and damper at either wheel axle. The spring and damper constants are inputs by the user together with the maximum extension and compression at each axle. Worth noting here is the linearity of this system due to the constants applied. Additionally, the weight of the vehicle is considered in the calculation as well as the position of the center of gravity. In figure 2.5 a schematic image of the model is shown, where h_{CG}, WB, WB_F, WB_R are the height of the center of gravity, wheelbase, distance to front and rear axles form the center of gravity, respectively. Additionally, springs k and dampers c, denoted as k_F, k_R, c_F and c_R, are presented, where the subscript F and R represents the front and rear, respectively.
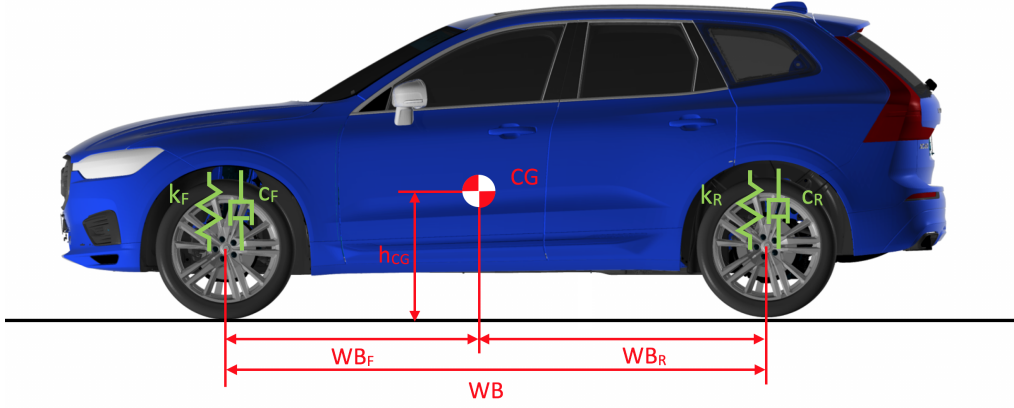
Figure 2.5: *Suspension model assumptions*

2.7 Relevant non-dimensional numbers

Two non-dimensional numbers are used in this thesis and presented below. The first one, the Froude number, Fr, is a dimensionless number used to characterise flow propagation. As an example, it is a powerful tool in order to determine wave propagation and sand bed formation. The number relates the inertial forces to the gravitational forces. The Froude number is defined as [19]:

$$Fr = \frac{v}{\sqrt{gh_m}} \tag{2.24}$$

Where v, g and h_m are the velocity of the flow, the gravitational constant and the hydraulic depth, respectively. The hydraulic depth is defined as the cross section area of the flow divided by the top width. Three different states of flow can be describe by the number: subcritical, critical and supercritical flow. In the case of subcritical flow the bulk flow is slow moving, allowing for wave propagation upstream. In the opposite case, the flow is sufficiently fast to hinder propagation upstream. In the transition between the two options, a critical state is reached. If a floating object is placed in the flow at this stage it would not move, either up- or downstream.

The second number, the Weber number, We, is a dimensionless number relating the inertial forces to the forces due to surface tension. The number is defined as [19]:

$$We = \frac{\rho v^2 L_{char}}{\sigma} \tag{2.25}$$

Where L_{char} is a characteristic length scale of the flow. This number will give an indication of the characteristics of the flow and the formation of droplets and breakups.

3   Method

The methods used for running the simulations of this work differs, depending on the employed formulation. In the case of VOF, the method includes geometry preparation, mesh generation, running the simulation and post-processing. Regarding SPH, all steps related to mesh generation are excluded. All steps mentioned above are presented in this chapter. Additionally, the method used during all physical tests are presented here as well. The study is divided into three major parts. The first part focuses on a comparative study between VOF and SPH, the second focuses on features of SPH while the third compares SPH and real-world tests. The water depth is the same in all simulation, 400 mm. In the first part, where VOF and SPH are compared a constant vehicle speed is used, 12 km/h. For the remaining parts, the vehicle speed differs between the tests. The range here is between 6 and 12 km/h.

3.1   Vehicle Configuration

Two vehicle models have been used for conducting all simulations in this study. A first model was used in the comparative study between VOF and SPH and where features of SPH were investigated. A second model was used during the comparative study between SPH and the physical tests. The reason for this was that in order to match the geometry of a physical vehicle with the simulations a new CAD model had to be imported. Both models were however of the latest generation of the XC60. This is an all-terrain vehicle with a higher ground clearance compared to models such as the V- and S-series. As was mentioned in the limitations of the thesis, neither of the configurations of the model are in production and differs from commercially available vehicles. The areas of extra interest on the vehicles were related to the front grille and the underbody. Regarding the simplified vehicle model, two shutters were located inside the grille. One upper and one lower. Both lead to the cooling system, including the radiator, condenser and charge air cooler (CAC). The upper shutter was kept close, while the lower one was kept open. This setup was chosen as it was the very setup used in StarCCM+ for previous simulations. The cooling system was blocked of, hindering water from passing through it. Exceptions were made to this setup in order to investigate the sensitivity of the influence of a modelled cooling package. The system was then approximated using a porous region. As no information about suitable parameters for the physics of this region was available, three setups were modelled, ranging from no to complete porosity. This is described more in section 3.8. In figure 3.1 the model used during the two first parts of this study is presented.

(a) *ISO view*   (b) *Side view*   (c) *Front view*
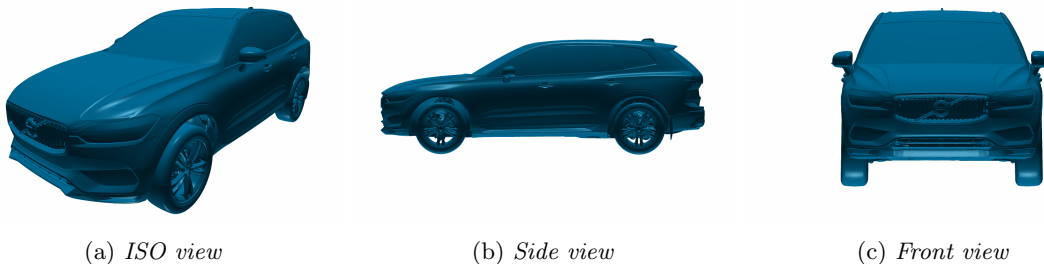
Figure 3.1: *The vehicle model used during the comparative study between VOF and SPH and while investigating the features of SPH.*

3.1.1   Boundary interpretation of parts and surfaces in the softwares

In StarCCM+ parts can be divided into separate regions, employing custom boundary conditions. In a pre-processing step parts can be split into Property Identifiers (PIDs), such as in ANSA. This information is imported into StarCCM+ and can be applied to split parts into separate surfaces. PreonLab uses a STL file format for all imported parts, hence all individual parts lose their information of PIDs. As a consequence, every part needs to be identified on a part based level. Every part is related to one boundary condition and data can only be exported for the whole part, e.g. in a post processing step. This needs to be decided before any geometry is imported into PreonLab.

As the same geometry was used in PreonLab as in the existing StarCCM+ setup, parts were exported directly from StarCCM+. If a different surface cell size was to be used, this had to be done in ANSA, where the size of the tessellation could be adjusted. A surface cell size of 1-4 mm was used for all parts in StarCCM+. This was not changed as the length scale of the cells were of the same magnitude as the particle spacing used in the SPH formulation.

3.2   Wading channel geometry

All simulations conducted in this study were based on the same wading channel geometry. The geometry was a replica of the real channel located at Hällered Proving Ground (HPG), VCCs test facility. Three different variants were however used. The channel had a 25 m test section with sloped side walls. For the comparative study between VOF and SPH the flat middle test section was extracted. This is described in section 3.3.1. While investigating feature of SPH the channel presented in figure 3.2 (a) was used. This was initially thought to be the channel geometry located at HPG. It was later found that the in and out ramps, located at the ends of the flat channel floor had a different inclination. This channel had an inclination of 4 degrees while the real channel only had 2 degrees, presented in figure 3.2 (b). This was corrected during the final part of the study while comparing SPH and real driving. This mistake did not affect the validity of this work due to the fact that the results from the different sections were independent.

(a) *Channel - 4 degrees inclined ramp*

(b) *Channel - 2 degrees inclined ramp*
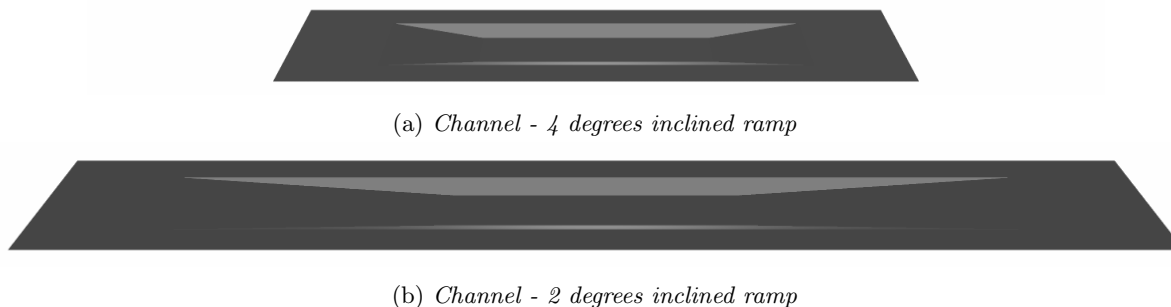
Figure 3.2: *The channel geometry which all simulations in the study have been based on. It consist of a 25 m long uniform test section. At the beginning and end of the section in and out ramps are located.*

3.3   StarCCM+ setup

In the following section the method implemented in StarCCM+ (ver. 12.06.010) is described, including mesh generation, solver settings, initial conditions and domain configuration. The described method was not developed in this work. It is however presented here due to its significance for the study. As a stationary mesh was used in the employed FVM formulation, a change of reference was performed. The vehicle was kept stationary, while the bulk of water was moving towards it.

3.3.1   Wading channel in StarCCM+

A simplified version of the channel presented in section 3.2 was used for conducting all VOF simulations in StarCCM+. Due to the change of reference, the in and out ramps were excluded from the setup, resulting in a uniform section. The length of the section was 22 m. The domain can be seen in figure 3.3. The inlet, upstream of the vehicle was simulated using a velocity inlet, the vehicle as stationary walls, the ground and sloped walls as moving walls, the outlet using a pressure outlet and the side walls and top of the domain using slip walls. As the inlet was used both for the water and air a condition using the volume fraction was implemented to determine where the respective phases were injected.
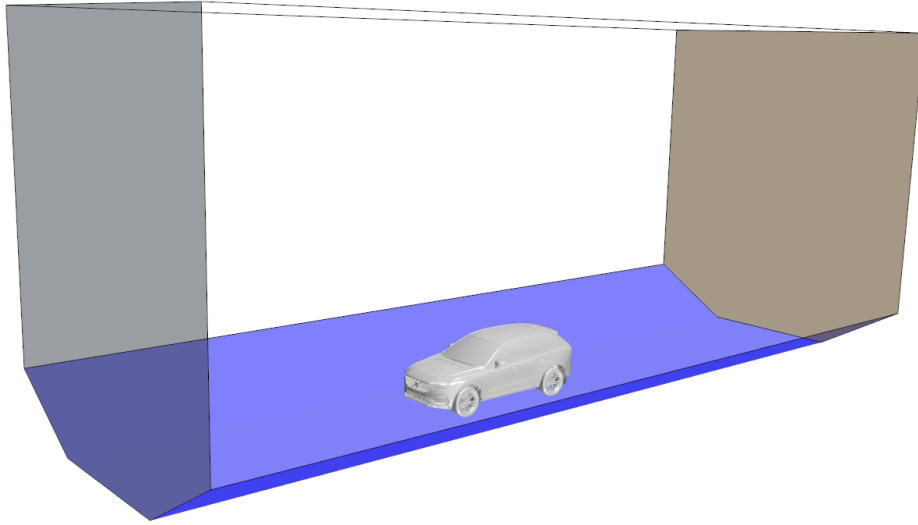
Figure 3.3: *The computational domain used in StarCCM+. It has a uniform cross section similar to the one found on the real channel found at HPG.*

3.3.2 Mesh

The meshing procedure consisted of four sequential steps, including a surface wrapper, surface remesher, surface repair and volume mesher. The surface wrapper was initially executed to replace the input CAD and fix potential problems connected to the geometry. The wrapper was followed by the remesher and repair tool to create the final surface mesh compatible with the volume mesh. The surface mesh on the vehicle had a base size in the range of 1-4 mm, depending on the area and requirements on refinement. For the volume, a hexahedral mesh was used resulting in 51,7 million cells. Refinement boxes with different base sizes were added in order to resolve smaller scales near the engine bay, underbody and wake area. A cross section of the volume mesh surrounding the vehicle can be seen in figure 3.4.
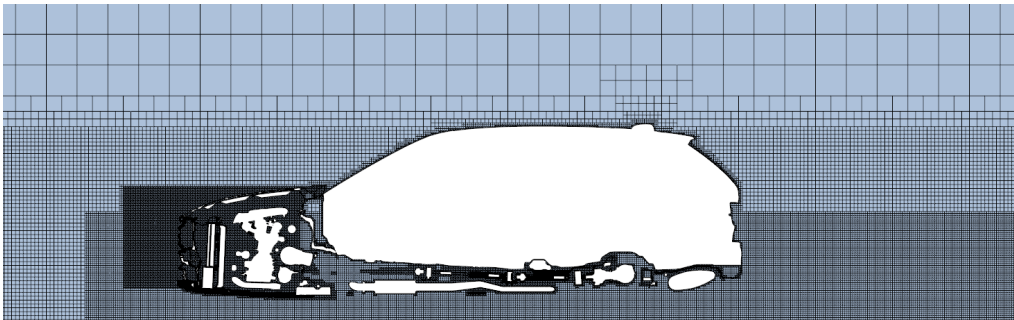
Figure 3.4: *Cross sectional view (y=0) of the volume mesh zoomed in around the car. As can be seen, different refinements in the mesh size are applied to different parts of the domain in order to capture all flow structures of interest, especially close to the engine bay and the underbody of the vehicle.*

3.3.3 Initial conditions

As the domain was stationary, a modified approach to account for the in ramp and increasing water depth was applied. This initial driving condition was simulated by introducing a wedge shaped body of water in front of the vehicle, with the same inclination as the ramp in the real channel. The height of the wedge corresponded to the full water depth defined in the simulation. This solution mimicked the behaviour of entering the channel,

Figure 3.5: *Initial volume of water present in the domain when the simulation was started, shown in turquoise. The water depth increases gradually as one progresses in front of the vehicle from zero to full wading depth. The image shows a cross section of the domain where much of the area aft of the vehicle has been cropped of.*

but differed in the transition between ramp and the flat channel floor. The initial bulk of water present in the domain, shown in turquoise, can be seen in figure 3.5. No consideration was taken trying to simulate the out ramp. The initial solution was applied using a volume fraction of water equal to one inside the turquoise area, while using a volume fraction of water equal to zero in the rest of the domain. An initial velocity field equalling the desired vehicle speed was implemented in the whole domain. The inlet was defined using a constant velocity throughout the whole event.

3.3.4   Simulation setup

The solver settings used in the setup was created by VCC to simulate wading conditions. The simulations were run unsteady, with a time step of 0.5 milliseconds, for 20 physical seconds. All settings used to conduct the simulations are given in table 3.1. One thing worth noting here is that no surface tension was modelled.

Table 3.1: *Implemented settings in StarCCM+*

CFD settings
Three dimensional
Implicit unsteady
Eulerian Multiphase
Multiphase Interaction
Volume of Fluid (VOF)
Multiphase Equation of State
Segregated flow
Gradients
Turbulent
Detached Eddy Simulation
SST (Menter) K-Omega Detached Eddy
Exact Wall Distance
All y+ Wall Treatment
Gravity
VOF Waves

3.4   PreonLab setup

In the following section the setup used in PreonLab is described, including the geometries, computational domain configurations and the physics. In terms of solver settings, the number of options in the SPH solver is more limited compared to StarCCM+. One obvious reason for this is the broader use of StarCCM+, suitable for a variety of simulation scenarios. The solver setting used in all simulations in PreonLab are presented in table 3.2.

Table 3.2: *Implemented settings in PreonLab*

CFD settings
Viscosity model: Morris [11]
Artificial viscosity: YES
Surface tension model: Pairwise Force [9]
Boundary handling: Gap
Adaptive timestep: YES
CFL number: 1
Maximal timestep: 0.5 ms

3.4.1 Wading channels in PreonLab

Three different wading channels were created and used in PreonLab. The first one had the purpose of replicating the conditions used in StarCCM+. This had an identical look compared to figure 3.3. The second and third ones were presented in figure 3.2. All three models where created in ANSA (ver. 17.01) and later imported into PreonLab. As all surfaces are interpreted as walls in PreonLab, the inlet and outlet were omitted in the first model to allow particles to enter and leave the domain. The rest of the walls, previously referred to as ground, side walls and top, were all included. The modelling method used for the two different reference frames and domains are presented below.

Stationary vehicle setup

The same reference frame was used in this setup as in StarCCM+ in order to replicate the conditions. The vehicle was kept stationary, while the body of water was moving towards it. The ground and sloped walls were given a moving wall condition equal to the simulated vehicle speed. The vehicle itself was considered as a stationary wall, with the exception of a constant rotational no-slip velocity condition on the rims and tyres. The computational domain was defined to exactly match the channel geometry.

A particle inlet, with the same geometry as the cross section of the channel was placed outside and upstream of the domain. The inlet velocity was set to equal the vehicle speed. As the particles exiting the inlet initially were outside of the computational domain a condition was defined forcing all particles in this region to have a fix, constant velocity in the negative direction of travel. This solution was decided as it would hinder particles from flowing back upstream and "fall" out of the domain. Particles adjacent, but inside, of the entering point to the computational domain hence felt the inlet point of the domain as a wall. Particles leaving the domain, at the outlet, initially re-entered their state of a constant velocity before being removed by a deletion zone. The deletion zone was place outside of the domain using the same reasoning as for the inlet. This solution was considered the most physically sound way of imposing the proper conditions in the domain.

Real-World setup

For this setup, the big advantages of SPH were shown and utilised. The channel was designed to replicate the whole real channel, including both in and out ramps. This body was kept stationary, using boundary conditions to simulate walls, while the vehicle was moving. The trajectory of the vehicle was determined using a Python (ver. 2.0) script provided by Fifty2. PreonLab has a built in Python compiler, where scripts can either be imported or written directly. The vehicle was initially placed outside of the channel, prior to the in ramp. The script defined the movement of the unsprung mass, including rims and tyres, to follow the shape of the channel. The wheels were also defined to rotate around their respective axles. The movement of the sprung mass was later related to the movement of the wheels. This division was introduced in order to allow for a suspension model to be implemented.

In order not to include the whole channel at every iteration in time, the computational domain was allowed to move with the vehicle. For most of the simulations in this study the size of this domain was set to be equal to the one used to mimic the conditions in StarCCM+. Deviations in the size of the computational domain were made in section 3.9, where the influence of the domain size was investigated. An inlet was placed in front of the domain, in the same manner as in the previous setup, moving with the vehicle speed. Particles were ejected through the inlet with the same velocity in the opposite direction of travel. This action cancelled out their movement leaving them hanging in space before the computational domain had reached them. Particles outside of the computational domain were not given a constant velocity, like in the previous setup due to the change of reference frame. A deletion zone was placed aft of the domain, also moving with the vehicle speed, to keep the number of particles down. A snapshot of the setup is presented in figure 3.6.

3.4.2 Simulated particle spacing

In order to investigate the influence of the particle spacing three different sizes were tested using the stationary vehicle setup. The particle spacings used were: 10 mm, 7.5 mm and 5 mm. The purpose of this study was to see how well the bulk flow was resolved, how well forces on exterior parts of the vehicle were modelled as well as how much water that accumulated in the air intake system (AIS). These were the three parameters that were used in the initial comparative study between VOF and SPH. For the rest of the study a particle spacing of 5 mm was used. The three parameters are presented below.
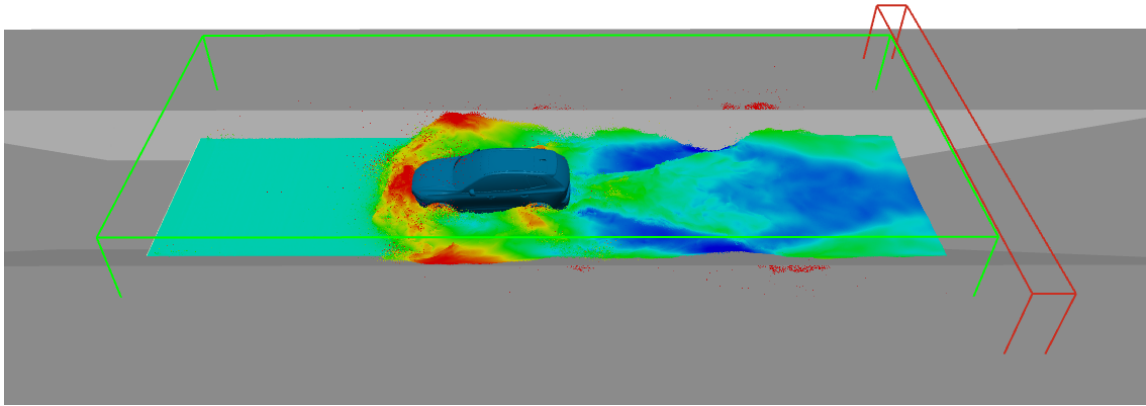
Figure 3.6: *A snapshot of the computational domain, bounded by a green box. Inside this box the particles are governed by the equations of motion. Particle are ejected using an inlet prior to the domain, left of the green box. The inlet is moving with the same velocity as the vehicle while ejecting particles in the opposite direction. Right of the green box, a deletion zone is located, bounded by a red box.*

3.5 AIS massflow

The AIS is located behind and besides the front grille. Air is fed through a duct leading from the area beside the radiator package inside the grille as seen in figure 3.7 (a). The air is led to a filter box presented in red in (b)-(c), from which air is fed into the engine. In order not to flood the engine it is important that the ingress of water into the filter box is kept to a minimum while driving. A drainage is located at the lowest part of the filter box. This can handle smaller volumes of water.

To get an estimate of the amount of water entering the AIS, a sensor plane was placed inside the duct connecting the area behind the grille and the filter box. In StarCCM+ this was done by defining a plane, similar in shape to the cross section of the duct. A report was defined, calculating the surface integral of the mass flux per second through the plane. In order to get the total contribution, the graph of mass flux was integrating in time. In PreonLab this was done by counting the total number of particles passing through the plane at every timestep, and then integrating the result in time. The shape of the plane in PreonLab was confined to be rectangular. The duct, on the other hand, was only roughly rectangular with rounded edges. Hence, if particles were close to the outside of the duct, these would have been added to the summation. The particles entering the system gave a positive contribution while particles leaving gave a negative contribution to the summation.

(a) *Front view*   (b) *Side view*   (c) *ISO view*
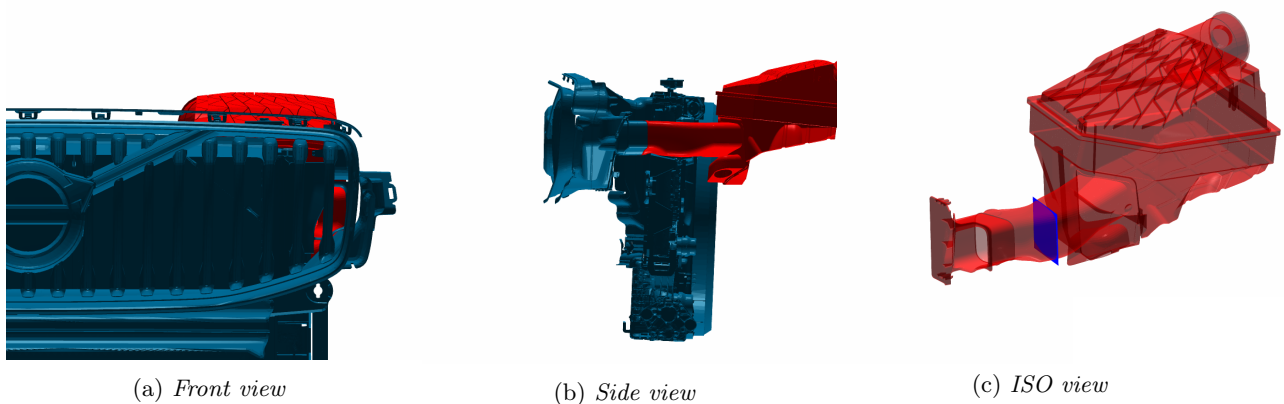
Figure 3.7: *Filter box and AIS duct as seen in PreonLab. In (a) the intake is visible through the front grille. The duct lead back beside the radiator package to the filter box, as seen in (b). The sensor plane, placed inside the duct leading to the filter box, is shown in (c), seen in blue.*

3.6 Free surface propagation

The method used for extracting the free surface of the flow differed between the SPH and VOF formulations. For visual purposes the particles, in SPH, were directly color coded by their position in the z-direction. In VOF, on the other hand, the interface was captured using the volume fraction. An isosurface was defined for a volume fraction of water equalling 0.5. The derived isosurface was later colored by a scalar function using the position in the z-direction. In figure 3.8 the instantaneous free surface is shown using VOF.

Surface height [m]

0.2   0.5   0.8
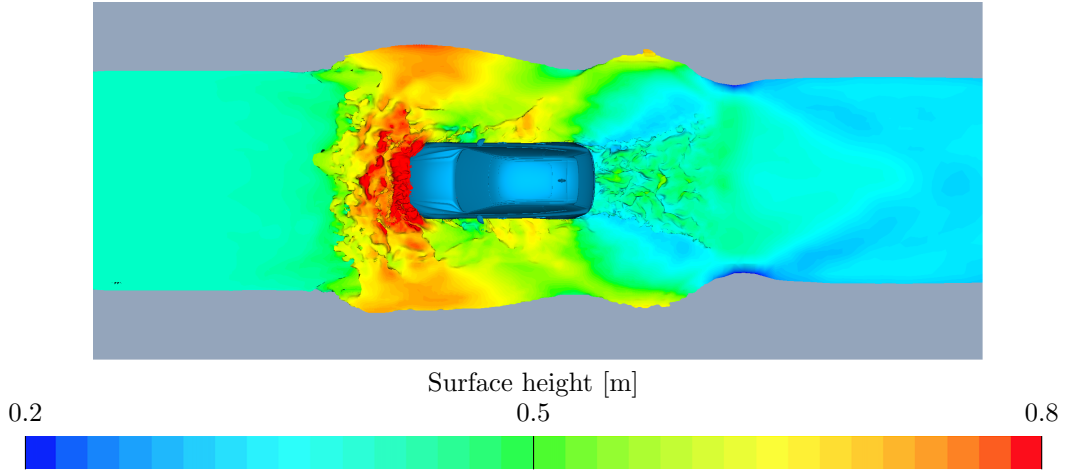
Figure 3.8: *The free surface taken as the isosurface of the volume fraction of water equalling 0.5, given in StarCCM+. The image is taken using an instantaneous field in time, using VOF, as seen from above.*

3.7 Forces on exterior panels

The drag and lift forces were measured on six different exterior panels on the vehicle, including the front, engine undershield and left and right hand side underbody panels and sidecarriers. All panels can be seen in figure 3.9. The drag forces were measured using both the VOF and SPH formulation in the comparative study, while the lift forces were only extracted while investigating the wake resolvement influence, presented in section 3.9. Two different force models where used in PreonLab to calculate the drag forces. One where the pressure of adjacent boundary particles were mirrored onto the surfaces and one where the pressure was calculated explicitly on the boundary particles. The two methods were tested in order both to see how they affected the total simulation time and how well they actually determined the forces.

(a) *Front view*   (b) *Bottom view*
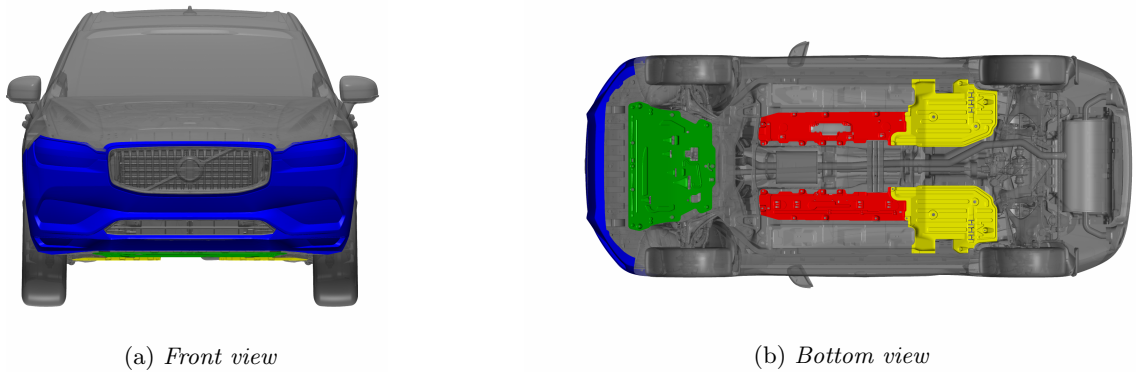
Figure 3.9: *Exterior panels used to do force calculations. Front in blue, engine undershield in green, sidecarriers in red and underbody panels in yellow. The sidecarriers and underbody panels are both divided left and right.*
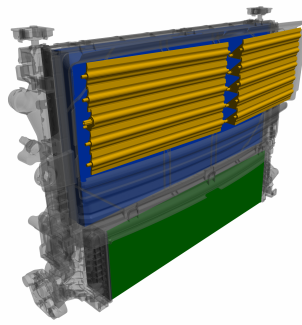
(a) *Radiator package*
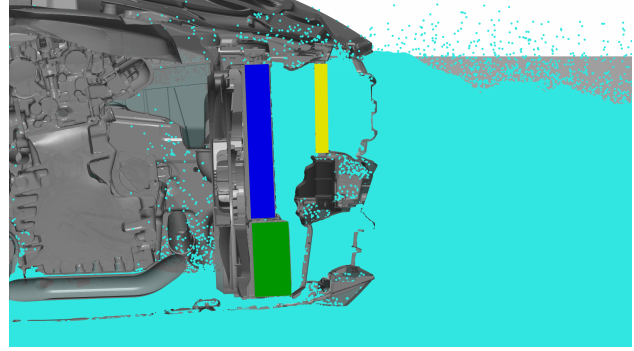
(b) *Cut plane (y=0) show the position of the package in the engine bay*

Figure 3.10: *The radiator package as a separate unit (a) and its position in the engine bay (b). In front of the shutter, seen in yellow, the upper grille is located. Water entering through the lower grille, sitting in front of the CAC in green, can propagate upwards to the area behind the upper shutter.*

3.8 Cooling system sensitivity

The radiator package was not modelled in the existing method in StarCCM+. The radiator, condenser, CAC and the upper shutter were all sealed of. In order to investigate the influence on bow wave formations due to partial or full allowance of water through the cooling system, six different configurations were tested. The cooling system was modelled using a porous region, but suitable values to set up this region were unknown and not investigated further in this work. PreonLab offered a porosity constant, in the range of 0 to 1, where 0 was equal to no porosity while 1 was equal to complete porosity. Three cases were designed, including the two extreme values and an intermediate value of 0.5. The same porosity constant was set to all parts. In order to model the radiator and condenser properly, these parts were merged into one thicker part, as seen in blue in figure 3.10. The reason behind this was that in order for PreonLab to interpret the parts correctly, a certain part thickness was necessary. The CAC, however, had a sufficient thickness by itself. This part is seen in green in the figure. For every porosity level the two cases of including the upper shutter or not were tested. The shutter is presented in yellow in the figure. If the upper shutter is opened, water entering through the upper grille will be able to continue to the cooling system, reducing the amount entering the AIS duct. However, the opposite might also happen, allowing water entering trough the lower grille to propagate upward and back out through the upper shutter. If this scenario plays out, more water is expected to enter the AIS duct. The outcome will be dependent on the ability of the cooling system to transport water away from the region between the upper and lower grille and the system itself. Both driving conditions, having open or closed shutters can occur, and are dependent on the engine temperature.

3.9 Computational domain optimisation

In order to reduce the number of computed particles in the calculations, the size of the domain was investigated. The upstream propagation, in front of the vehicle, was assumed to be dependent on the Froude number. If a subcritical value is achieved the wave will propagate upstream faster than the vehicle is moving. If, on the other hand, the Froude number is supercritical, the vehicle will always break the wave. The latter option allows for a less computationally heavy approach, where a smaller volume of water needs to be accounted for in the calculations. In the former case the computational domain needs to take this upstream propagation into account. The same reasoning can be applied to the wake, downstream of the vehicle. If no upstream influence is noticed, in terms of altered wave patterns upstream, it is not necessary to be resolved. The side walls of the channel will have some influence in the build-up of the wave due to their confining effect of the laterally propagating parts of the water. This will push more water upstream but was not investigated further here.

This part of the study was divided into two parts. One where the rear of the domain was reduced in order to investigate a upstream influence and one where the vehicle speed was altered to see how that would affect the upstream propagation in front of the vehicle.

Regarding the first section, four different domain sizes were constructed. The largest one had the same

19

dimensions as the previously used domains, 22 m. For the remaining three the wake resolvement was reduced, resulting in domains of the lengths 18, 14 and 11.5 m. The smallest domain ended right after the rear bumper of the vehicle. Two parameters were used to investigate the influence of the wake resolvement: lift forces on the exterior body panels and the free surface at one instance in time. For this particular part of the study only one vehicle speed was used, 12 km/h. This created a supercritical Froude number.

For the second part of the domain optimization study the vehicle speed was altered in order to investigate how that would affect the upstream propagation. Seven different vehicle speeds were used in the range between 6 and 12 km/h. The criteria used to determine the upstream propagation was the distance, in the x-direction, the front wave had travelled upstream the moment the inlet no longer ejected particles into the domain. This resulted in lengths measured at different instances in time.

3.10   Wading at HPG

In this section the procedures and setups used for the conducted physical tests are presented. The experiments were performed at HPG. The main purpose of the physical tests were to create an environment where suspension movement data and water propagation could be observed. The same setup was later recreated in PreonLab. A new vehicle was used for these tests. It was of the same model as before, but with new exterior parts, engine and rims.

3.10.1   Test setup

The vehicle used in the physical tests was not the same as the one simulated in the rest of this work. This was a consequence of the fact that the available vehicles, with the sensors needed, were not know at the beginning of this thesis work. The model used to replicate the real world condition in PreonLab was however identical to the real one.

Minor modifications were made to the vehicle before the tests were conducted. The hood was removed in order to allow for a disconnection of the filter box. A new hose was connected to the engine air intake, leading to the roof, eliminating the risk of engine water intake. The setup, with the removed hood and additional air intake hose can be seen in figure 3.11 (a). The weight, with two people in the front seat, was recorded. This was done using one scale for each wheel. The weight distribution, axle wise, was found to be 51.6 % forwards. The weight of the wheels themselves were also recorded, as they did not contribute to the sprung mass of the vehicle. More parts of the suspension should technically be considered unsprung mass, but were neglected as they were considered to belong to the sprung mass in PreonLab to simplify the kinematics. A camera was placed standing next to the end of the channel to film the bow wave formation.

During the tests, two parameters were sampled. The first one was the vehicle speed. This was logged through the rotation of the wheels. One signal was sent from each wheel, but data was only collected from the front right, as they were assumed to all be the same. The second parameter was the damper positions, for all four wheels. This data was collected through the sensors used in the air suspension system present in the vehicle. This gave the compression and extension of all four wheels. This was assumed to equal the wheel travel in the ground normal direction. All data was sampled with a frequency of 50 Hz. The height of the wheel arches were measured beforehand, in order to be able to tune the simulation model to match the real height setup.

In order to be able to match the movement in the physical tests and PreonLab as accurately as possible a new driving setup was chosen. Instead of driving into the channel with a constant speed, the vehicle was placed on the in ramp allowing the front wheels to just touch the waterline. The test started with the vehicle standing still, followed by an acceleration to the desired speed. This would allow for a precise match in speed and position along the channel during the implementation in PreonLab.

The water depth was kept constant at 400 mm, with an estimated error of ±20 mm. The main error in the deviations was due to the fact that the whole body of water in the channel was moving back and forth for a long period of time after each test. The channel was refilled manually after each test due to losses from spilling while leaving the channel and the water height was measured using a measuring stick.

Four tests were conducted. During the first test, a vehicle speed of 6 km/h was strived for. This would guarantee a subcritical Froude number. The second test was done at 12 km/h to produce a supercritical Froude number and with large dynamic bouyancy effects. During the first two tests the vehicle was moving in the middle of the channel, having an equal distance to the right and left hand side sloped walls. The third test was performed in order to investigate the sensitivity to deviations in the y direction while driving. The vehicle

(a) *The test car*
(b) *The wading channel*

Figure 3.11: *The car used in the tests and the wading channel. The hood of the car is dismounted to allow for an extension to attach to the air intake. The hose used for this purpose can be seen following the left a pillar.*

was aligned with the left side of the channel, where the outside face of the left wheels matched the bottom of the left sloped wall. The speed strived for was once again 12 km/h. It was proving difficult to maintain a constant speed due to the large external forces on the vehicle during the first three tests. The resulting speed was around ± 1 km/h the intended. In the fourth and final test the vehicle was placed in the middle of the channel in order to measure the static buoyancy effects. Data was measured over 10 seconds and averaged.

3.10.2 Simulation setup

The vehicle used during the physical tests was exported directly from the CAD database in order to get an exact match in the geometry. No modifications were made to the model more than removing the hood. The front and rear static height were adjusted according to the measured values from the real vehicle. The suspension model was implemented using the vehicle weight, center of gravity, front and rear suspension extension and compression as well as spring and damper coefficients. The coefficient were linearized as the force curves were found to be nonlinear. These approximations were however considered valid as the behaviour of the system in the travel range measured during the physical tests was proving to be more or less linear. This was the greatest source of error in the simulations apart from the fact that that no tire deformation was taken into account.

The vehicle was placed next to the channel allowing the front wheels to just touch the waterline, just as in the real tests. The same computational domain, 22 m long, as for the rest of this study was used here. One exception to the domain size was made in the first test extending it 2 m upstream to capture to full upstream wave propagation occurring at this speed. The logged vehicle data was imported and applied to the wheelbase, the computational domain, the inlet and the deletion zone. This made sure all bodies moved in accordance with the actual tests. The speed was converted to allow for the correct rotation of the front and rear wheels. Apart from the tires and rims, wheel bolts, brake discs and calipers were assigned as unsprung parts. The brake disc were also allowed to rotate with the wheels. The vehicle model used in these simulations can be seen in figure 3.12.
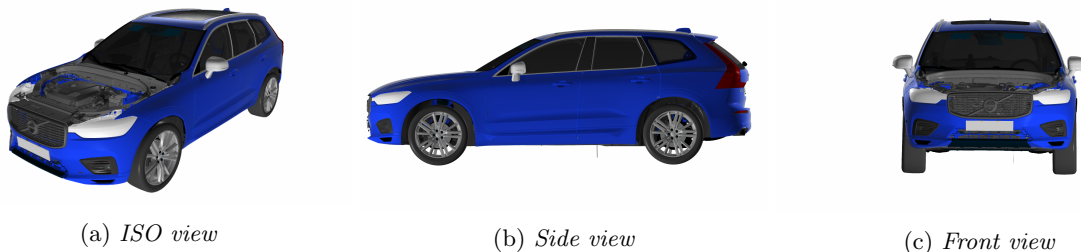
(a) *ISO view*
(b) *Side view*
(c) *Front view*

Figure 3.12: *The vehicle model used in the simulation setup with the purpose of replicating the real condition during the physical tests.*

The simulations were run until the vehicles had all reached the same position on the out ramp, resulting in three different physical simulation times. The two cases travelling at 12 km/h, middle and side, resulted in 21.4 seconds and 22.1 seconds, respectively. The case of a lower speed resulted in 29.8 seconds of physical simulation time. The two faster cases agrees well with the simulation time of the previously presented StarCCM+ setup, running at the same speed.

For the forth simulation, measuring the static dynamic effects, the vehicle was placed in an empty box, just barely larger than the vehicle itself. Particles were later injected to fill the surrounding volume to the correct height. This method was chosen as it would guarantee no particles ending up inside the vehicle falsifying the results. Once the correct depth had been reached, the suspension data was measured and averaged over 10 physical seconds of simulation time.

4 Results

In this chapter the acquired results from this study are presented. Main focus is devoted to pure results, while some discussion is intertwined. The next chapter is a continuation, where the discussion is more elaborate. The present chapter is divided into three section. The first focuses on the comparative study between SPH and VOF, the second on the features of SPH, including the domain size and radiator modelling, while the final presents the results from the real tests and corresponding SPH simulations.

4.1 VOF SPH comparison

In this section the results from the initial comparative study between VOF and SPH are presented. The simulations in PreonLab where conducted using three different particle spacings: 10 mm, 7.5 mm and 5 mm. The three cases were compared to a VOF simulation using a setup, with the purpose of replicating the conditions of SPH. This included geometry, initial and boundary conditions. Two different force models were tested using SPH. One simplified where particle pressures were projected onto walls and one where they were calculated explicitly. Simulation run times and the average number of particles for all simulations are presented in table 4.1. As the particle spacing is reduced from 10 to 5 mm, the number of particles increase eight times as expected. The simulation run time does however increases almost ten times, using the simplified force model. This increase is less significant using the explicit force model. The simulation run time using VOF is far greater than any of the SPH simulations. The same number of computational cores were used for all seven simulations, namely 1232 cores.

Table 4.1: *Run times and number of particles for the simulations with the intention of replicating the setup used in StarCCM+. The number of particles have been averaged over the whole simulation events. By changing from the simplified force model to the explicit, an increase in simulation run times can be observed. This increase is more significant at larger particle spacings. The simulation run time at 5 mm is approximately ten times that using 10 mm, while the number of particles only increase by eight times.*

	10 mm	7.5 mm	5 mm	VOF
Mirror pressure [CPUh]	6232	10004	61686	-
Explicit pressure [CPUh]	12935	14784	63550	-
Simulation time [CPUh]	-	-	-	151124
No. of Particles (averaged)	41 000 000	98 000 000	337 000 000	-

4.1.1 Free surface propagation

The free surface in the full domain is shown at two instances in time in figure 4.1 (a)-(h). In the figure, the three different particle spacings in SPH and VOF are presented. The surfaces are colored by height. Observing figure 4.1 (a)-(d) the initial build-up of water has the same behaviour in all four images. A bow wave is formed, propagating outwards and up the sloped walls. The same upward propagation can be seen in all cases. Some of the structures beside the vehicle are smoothed out in VOF. Aft of the vehicle, lower water levels are seen. A diverging v-shaped stern wave, starting from the rear of the vehicle is seen in all images. This is however more evident in the SPH simulations. It is followed by a converging structure, also seen in all images. This is also better captured in SPH. Different structures, with higher and lower water marks can be seen at the outlets in SPH while the waterline is more uniform in the VOF simulation. This can be described by the coarser volume mesh in this region which smears out the solution.

At 20 seconds, presented in 4.1 (e)-(h), the same overall behaviour can once again be seen in all images. The upstream propagation is strengthened by a decreasing particle spacing. The most significant upstream propagation can be seen in VOF but is closely followed by the 5 mm SPH solution. The same reasoning regarding the wake can be applied here as well. The solution is smoothed out close to the outlet in VOF while the same solution accuracy is maintain in SPH. No large differences can be observed between the different particle spacings in SPH. This holds well for the bulk flow. The overall behaviour is independent of particle spacing. Looking at a finer scale, small structures tend to be smoothed out while using a larger particle spacing.
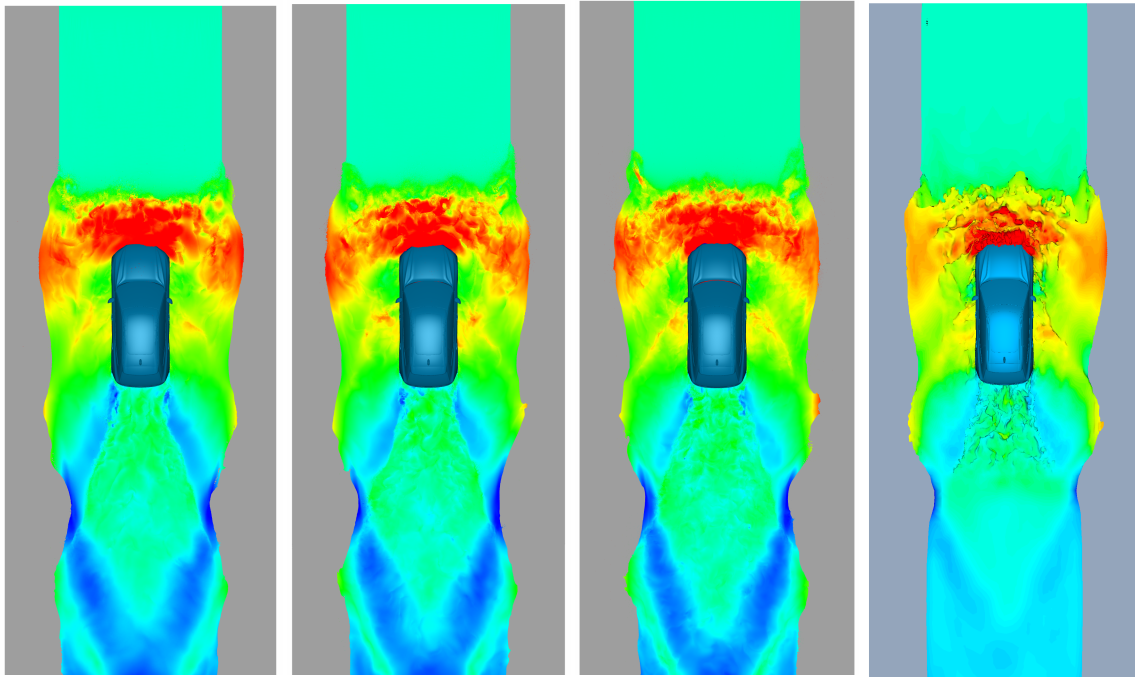
(a) *Spacing: 10 mm*
Time: 10 s

(b) *Spacing: 7.5 mm*
Time: 10 s

(c) *Spacing: 5 mm*
Time: 10 s

(d) *VOF*
Time: 10 s
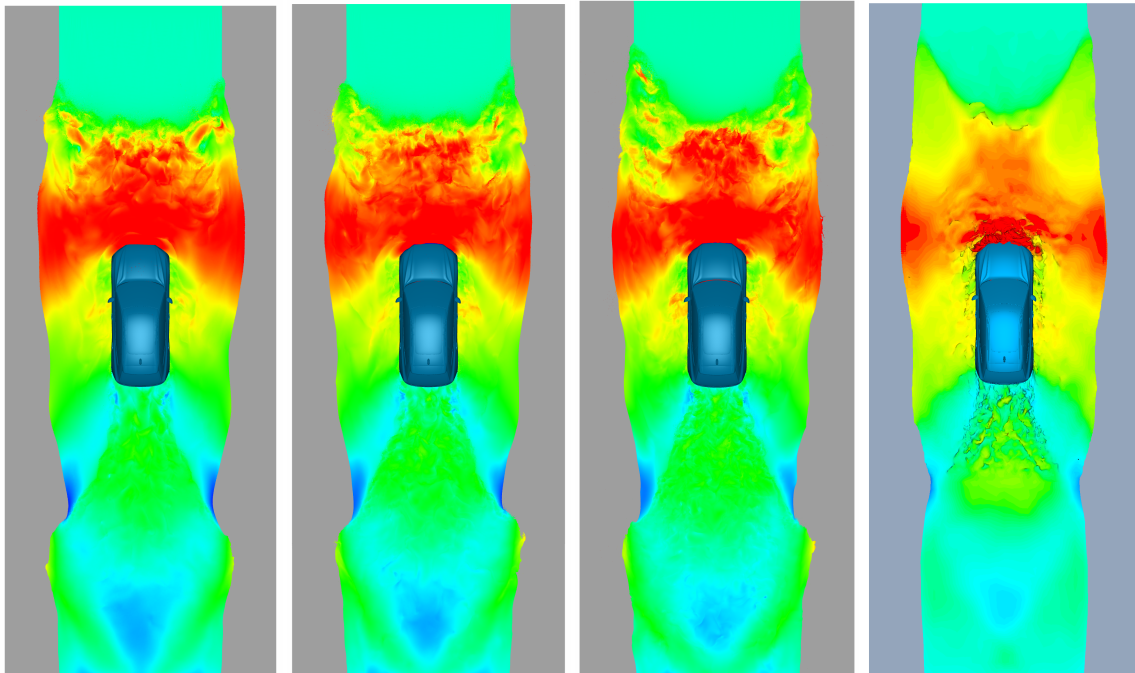
(e) *Spacing: 10 mm*
Time: 20 s

(f) *Spacing: 7.5 mm*
Time: 20 s

(g) *Spacing: 5 mm*
Time: 20 s

(h) *VOF*
*Time: 20 s*

Surface height [m]

0.2
0.5
0.8
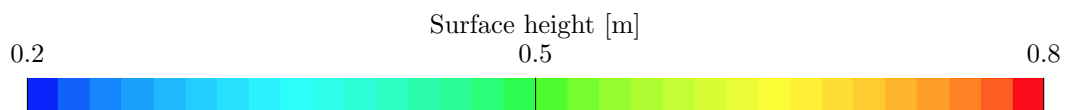
Figure 4.1: *Stationary vehicle setup for both VOF and SPH, with three different particle spacings. 10 mm, 7.5 mm and 5 mm. The surface is captured at 10 and 20 seconds of physical simulation time.*

24
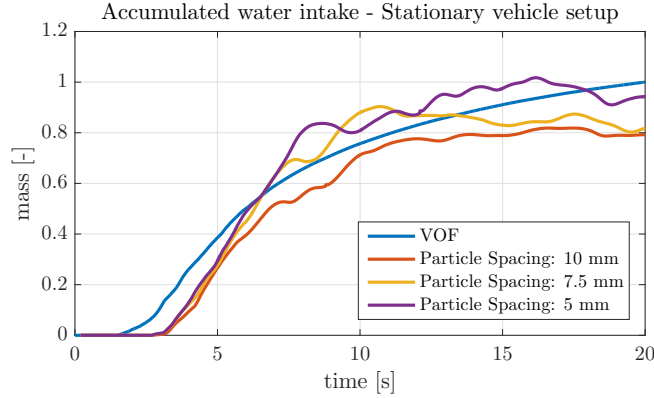
Figure 4.2: *Accumulated mass of water entering the AIS, calculated for both SPH and VOF. Water enters the duct earlier in the case of VOF. The results have been normalized by the final mass of water in the AIS taken from the VOF simulation.*

4.1.2 Water intake AIS

The mass of water entering the AIS is presented in figure 4.2. As can be seen in the graph, all four simulations render similar results. An increase in the mass can be seen with decreasing particle spacing. Larger fluctuations, in the amount of water entering and exiting is observed using a finer particle spacing. Water start to enter the system earlier using VOF, while no difference can be seen between the SPH cases. Two possible explanations for this are that the bow wave formation differs between VOF and SPH and that the position of the sensor plane inside the duct differs slightly. The different results in SPH could be explained by the difference in the resistance the particles experience while penetrating the narrow gaps in the upper grille. This region has the most narrow gaps the particles have to encounter on their way to the AIS.

4.1.3 Forces on exterior panels

The resulting forces calculated on the six studied panels can be seen in figures 4.3 and 4.4. In figure 4.3 the simplified force model is presented while the explicit force calculation is presented in figure 4.4. As the body of water initially hits the vehicles, peak values in the forces are observed, larger and less stable than the state found later during the simulations. As can be seen in all twelve graphs, the forces in SPH are overpredicted compared to the ones calculated using VOF. The relative difference is most prominent in figure 4.3 (b) and 4.4 (b), where the resulting values of the forces in the SPH simulations seem to converge to values more than twice the ones found in the VOF simulations. One explanation to this could be that the prediction of the build-up of water and the resulting waterline in front of the vehicle differs between between the two frameworks.

What is more interesting is the decrease in the estimations of the forces as the particle spacing is reduced. This is most evident in figure 4.4 (a), but the trend is seen for all studied components. Moreover, this trend is also stronger for the panels located near the front of the vehicle. One possible explanation for this is that the normal stresses, which are dominant in the front, needs a finer particle resolution in order to converge compared to the shear stresses, which are dominant under the vehicle. Another observation is that this trend is stronger for the explicit force calculation in figure 4.4. The reason for this is not known. The different force models in SPH also seem to converge to different values.

Fluctuations in the forces are expected in SPH, as described in section 2.4.7. These fluctuations can be seen in all results and are much larger than those found in VOF. The fluctuations seem to be of the same magnitude, independent on the force model used. Differences can be seen in the force predictions between the right and left pairs of the underbody panels and sidecarriers. This observation can be seen in both SPH and VOF, but is expected, due to that the vehicle underbody is not completely symmetrical.

(a) *Front*

(b) *Undershield*

(c) *Sidecarrier LHS*

(d) *Sidecarrier RHS*

(e) *UBP LHS*

(f) *UBP RHS*
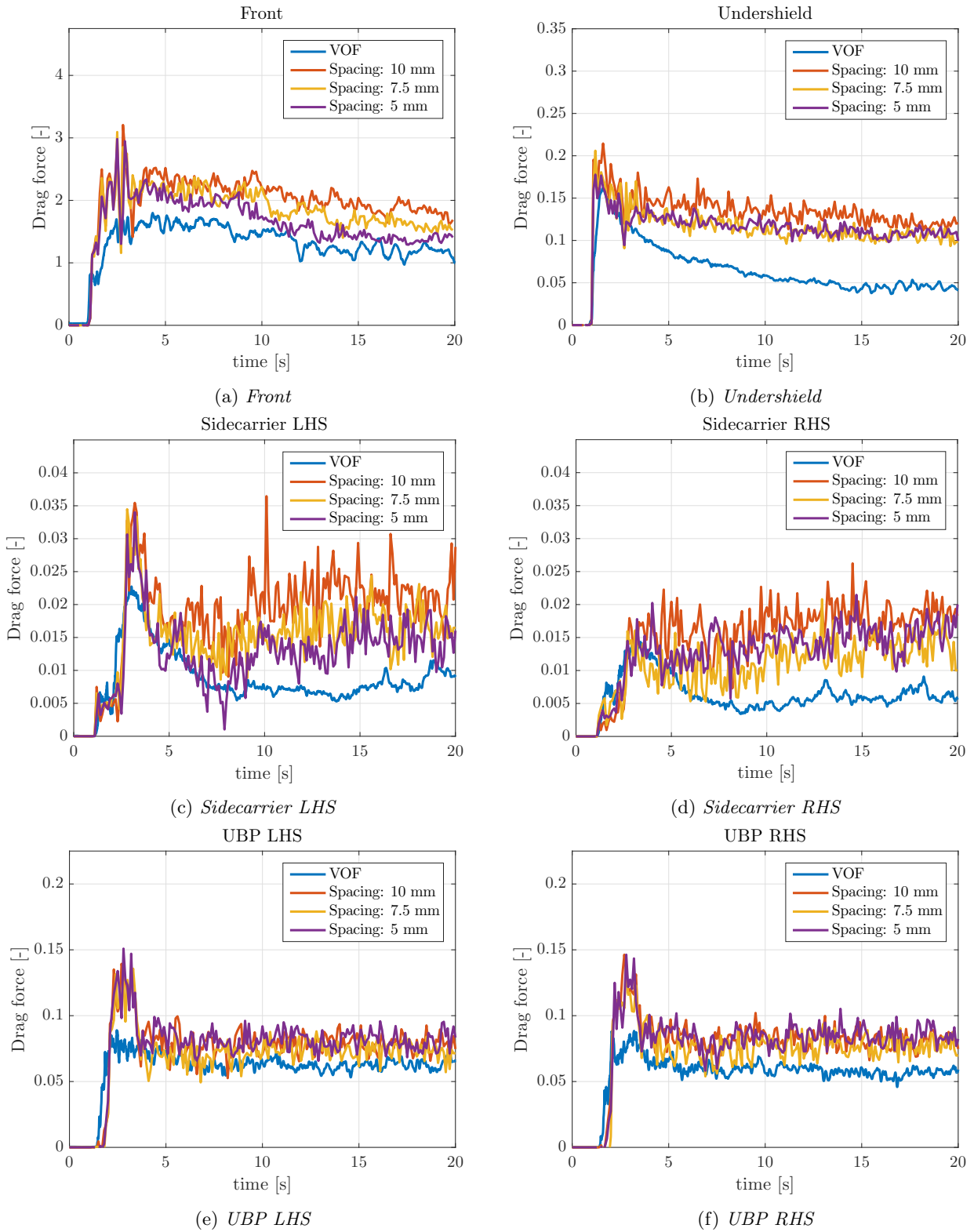
Figure 4.3: *The measured drag forces on the six panels for both VOF and SPH using the simplified force model. SPH overpredicts the forces compared to VOF. Furthermore, fluctuations in the forces are more prominent in the cases of SPH. This behaviour comes as a consequence of the formulation, as was described in section 2.4.7. The forces have been normalized by the magnitude of the instantaneous drag force on the front panel of the VOF simulation at 20 seconds using the simplified force model.*
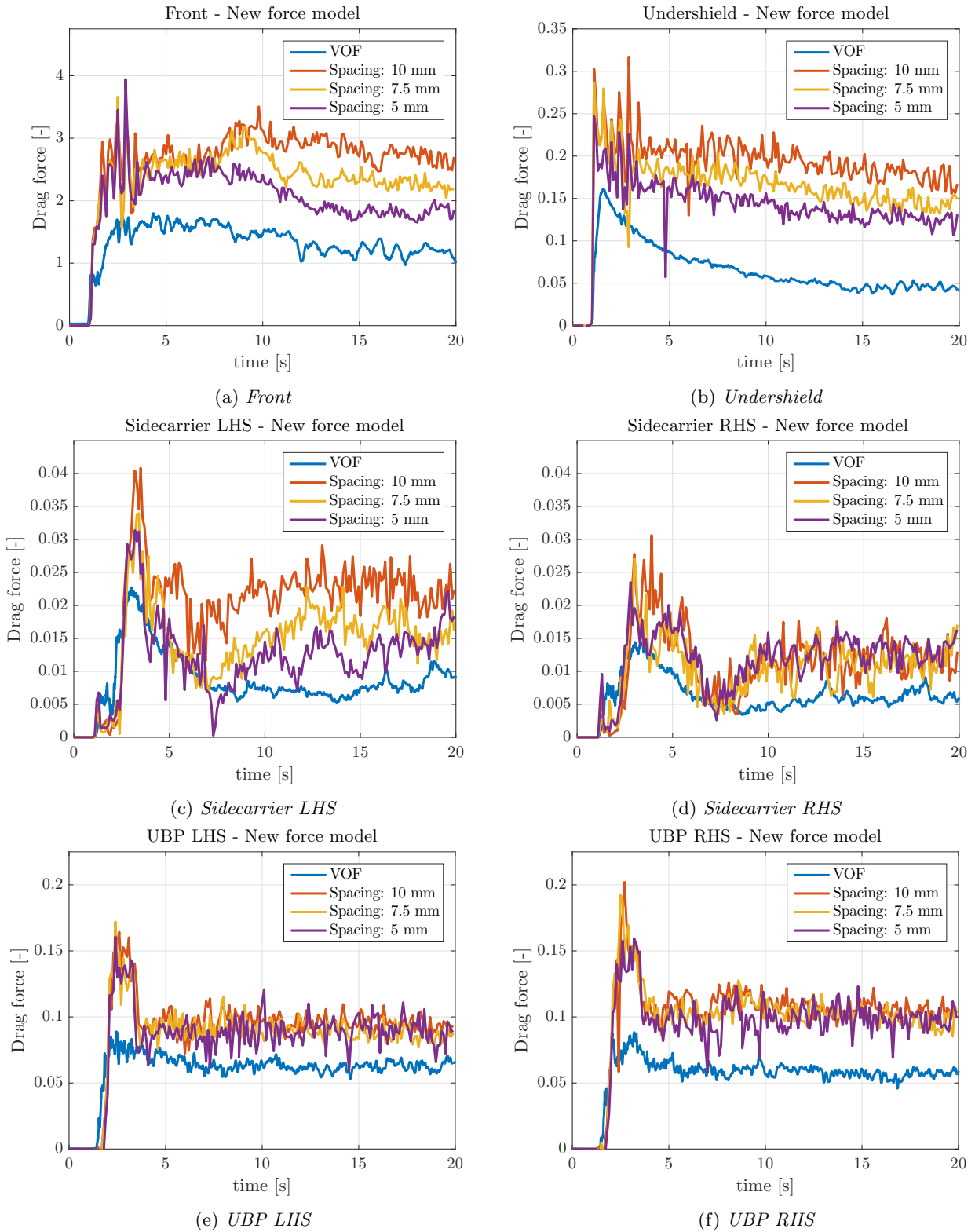
Figure 4.4: *The measured drag forces on the six panels for both VOF and SPH using the explicit force model. This model seems to converge to values higher than the previously presented one. Larger differences can also be observed between the three particle spacings. The forces have been normalized by the magnitude of the instantaneous drag force on the front panel of the VOF simulation at 20 seconds using the simplified force model.*

4.2 Computational domain configurations

In this section the results from the domain size investigation are presented. Initially, the upstream propagation as a function of vehicle speed is presented. Seven different vehicle speeds are tested in the interval between 6 and 12 km/h. This is followed by the investigation of the influence of the domain length aft of the vehicle. Both the free surface propagation at one instance in time and lift forces on underbody panels are accounted for. Only one vehicle speed is used, 12 km/h.

4.2.1 Upstream propagation

In figure 4.5 (a)-(g) the upstream propagation for the seven different vehicle speeds are presented. The snapshots have been taken at different instances in time. The criteria used to decide the time was the moment the upstream propagating wave reached the point on the out ramp where the inlet no longer injected particles in to the domain. For a decreasing vehicle speed, the distance the wave travels upstream increases gradually. The switch from super to subcritical flow lies somewhere between 8-9 km/h looking at the figures, which is higher than the calculated, theoretical critical vehicle speed of 6.67 km/h. This will have a great impact on the minimum computational domain and the overall simulation time. For supercritical cases the channel can be prolonged while using a constant domain size. However, for the subcritical cases the resulting domain lengths have to account for this as the waves will continue to propagate upstream.

(a) *12 km/h*	(b) *11 km/h*	(c) *10 km/h*	(d) *9 km/h*
Fr = 1.80	*Fr = 1.65*	*Fr = 1.50*	*Fr = 1.35*
2.46 m	*2.28 m*	*2.87 m*	*3.70 m*

(e) *8 km/h*	(f) *7 km/h*	(g) *6 km/h*
Fr = 1.20	*Fr = 1.05*	*Fr = 0.90*
4.82 m	*6.16 m*	*6.70 m*

Surface height [m]

0.2   0.5   0.8
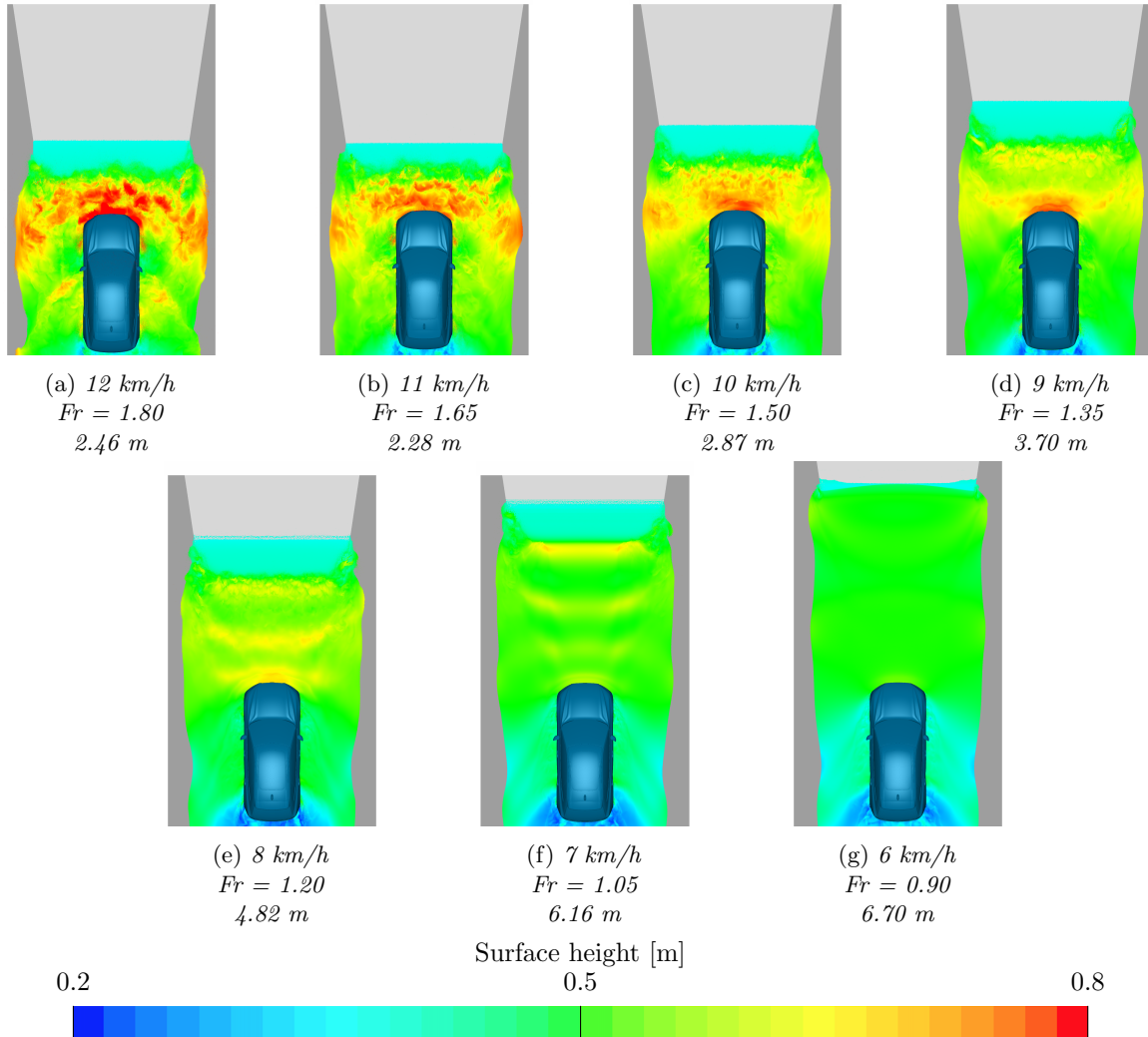
Figure 4.5: *Resulting upstream propagation for different vehicle speeds. By reducing the vehicle speed the bow wave propagates further upstream before the inlet stops injecting particles in the channel.*

4.2.2 Wake resolvement

The size of the domain rear of the vehicle is investigated in order to reduce the computational time. In figure 4.6 the wake of the four different domain sizes are presented. Observing the images, no major difference in the structures can be seen. Comparing (a) and (b), the same wake pattern is present. The same can be observed comparing (a) and (c). In (d), where none of the wake is taken into account, the structures on the sides of the vehicle are still unchanged. This suggest there is minor upstream influence on the wake at this vehicle speed.

(a) *Length: 22 m*   (b) *Length: 18 m*   (c) *Length: 14 m*   (d) *Length: 11.5 m*

Surface height [m]

0.2   0.5   0.8
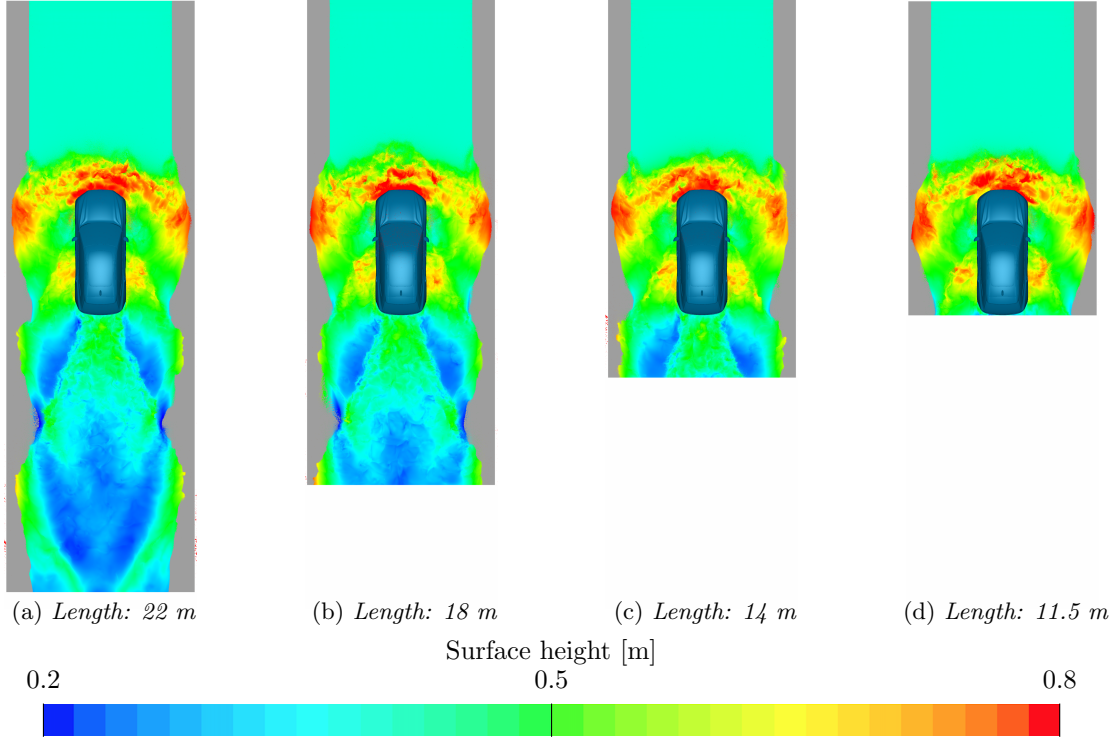
Figure 4.6: *Free surface colored by height for the four different domain sizes used to investigate the influence of the wake in the simulation. No major differences can be observed comparing the four cases.*

The same reasoning can be applied looking at the lift forces on the six panels presented in figure 4.7. No major differences can be seen here either. The noise introduces some differences in the signals, most clearly between 5-10 seconds of the simulations. This is expected due to the randomness in the small structures of the flow fields. The peak values observed at the initial impact with the water have different amplitudes, but all features occur at the same instances in time. The forces tend to increase in time while moving through the channel until reaching the out ramp. This could be explained by the gradual build of the of wave pattern throughout the simulation event. The rear most panels, the underbody panels, left and right, lies within one meter of the outlet in the case with the shortest domain. Comparing the right and left hand sidecarriers, larger forces are experienced on the right side. This can be explained by that they are not completely symmetric.

Big differences were observed in the upstream wave pattern for different vehicle speeds, presented in section 4.2.1. If this is applied to the wake, going at a lower speed, larger influences on the pattern near to the car are expected. By not resolving the wake, structures developing aft of the vehicle will not be considered, which might drastically change the behaviour of the flow closer to the vehicle.

Looking at the simulation run times, presented in table 4.2, the number of cores used seem to have a great impact on the simulation run times. Increasing the number of cores is less effective, for this particular case.

Table 4.2: *Simulation run times using different domain lengths.*

Domain length [m]	22	18	14	11.5
Cores [-]	1232	2160	984	1232
Simulation time [CPUh]	32853	51840	19680	23408
No. of Particles (averaged)	199 000 000	171 000 000	139 000 000	118 000 000

(a) *Front*

(b) *Undershield*
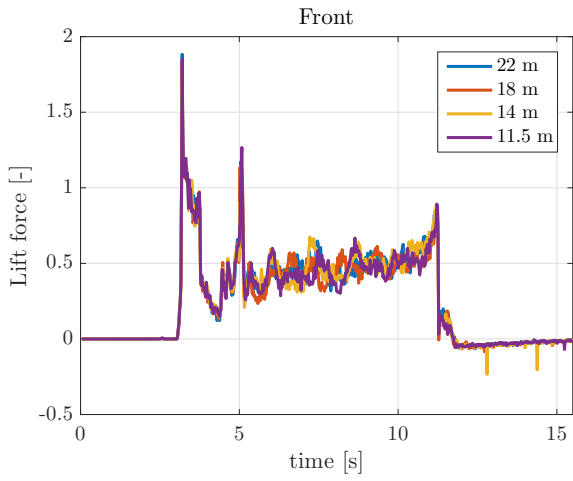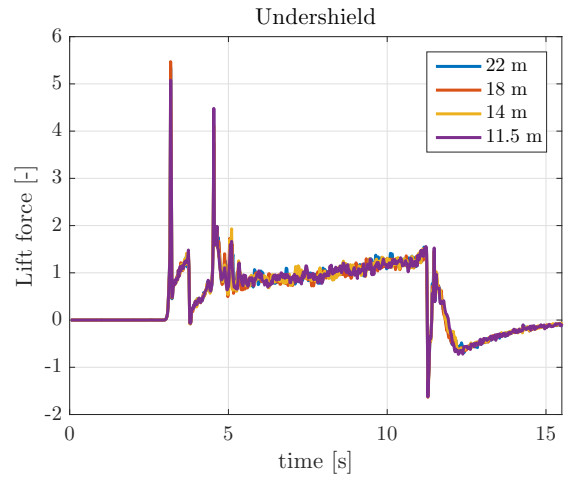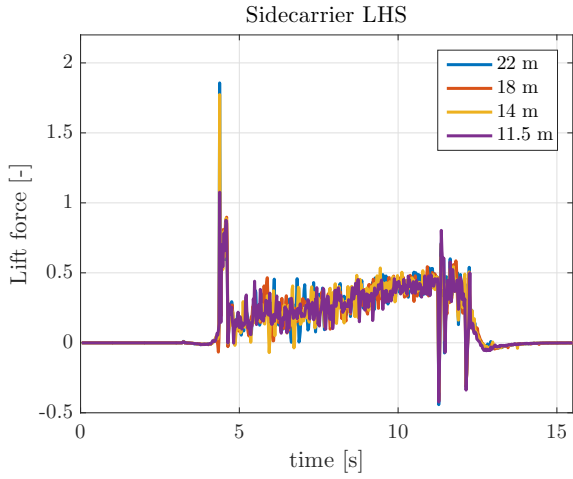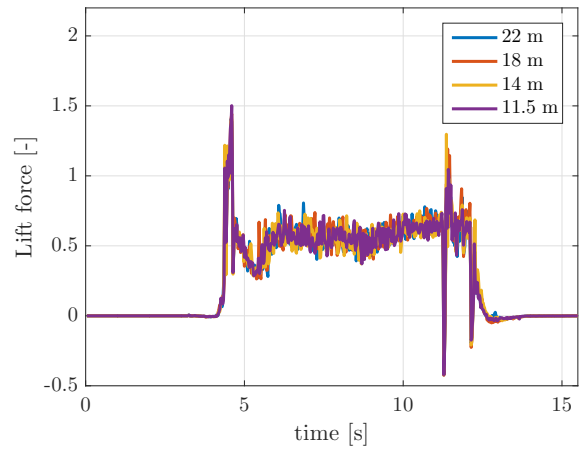
(c) *Sidecarrier LHS*

(d) *Sidecarrier RHS*
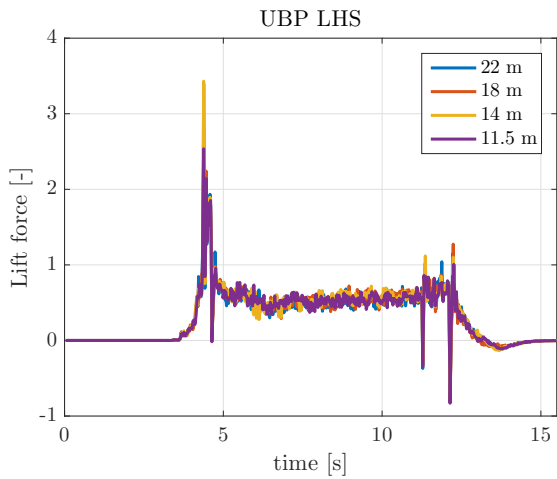
(e) *UBP LHS*
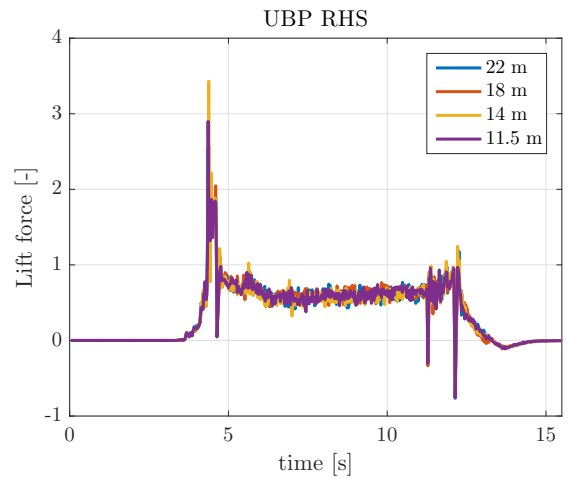
(f) *UBP RHS*

Figure 4.7: *Lift forces on the six panels for the four domain sizes tested. The same behaviour can be seen in all simulations, including all panels. Peak values are observed, but they occur at the same instances in time. The forces have been normalized by the magnitude of the instantaneous drag force on the front panel of the VOF simulation at 20 seconds using the simplified force model.*

4.2.3 Radiator sensitivity

Observing the influence of the radiator and upper shutter both parameters seem to have a big impact on the final AIS water intake. Looking at figure 4.8 (a)-(f), showing a cut plane ($y=0$) the porosity of the radiator package determines how the engine bay is flooded. By keeping the radiator completely shut no water passes through, while some water is still entering the AIS area from below. By modelling the radiator using complete porosity, the waterline stays unaffected when comparing the level in front and aft of it. The upper shutter will lower the waterline in front of the radiator, most clear comparing figure 4.8 (c) and (f). Using the same sensor


(a) *Porosity: 0, Shutter: NO*   (b) *Porosity: 0.5, Shutter: NO*   (c) *Porosity: 1, Shutter: NO*

(d) *Porosity: 0, Shutter: YES*   (e) *Porosity: 0.5, Shutter: YES*   (f) *Porosity: 1, Shutter: YES*

Position z [m]

0.2   0.5   0.8
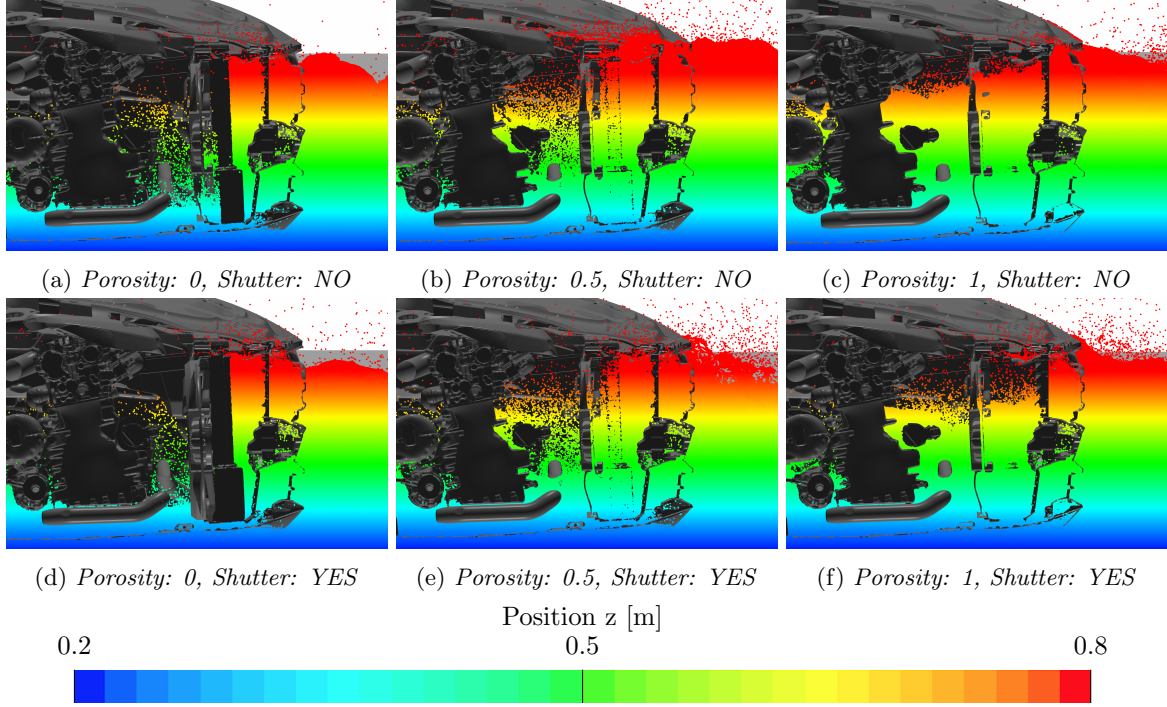
Figure 4.8: *Cut plane (x-z) through y=0 showing the effect of water entering the engine bay by modelling the radiator and removing the upper shutter.*

plane inside the AIS duct as before, the final mass of water entering the system can be monitored. In figure 4.9 the six previously presented cases are shown. The porosity seems to affect the final mass of water more than the shutters. The shutter itself does however affect the peak values in the amount of water entering. No trends can be observed, as more water enters while increasing the porosity from 0 to 0.5 and decreases continuing from 0.5 to 1. Some differences can be observed comparing figure 4.9 with figure 4.2. While on the out ramp of the wading channel, some water is drained, which is not taken into account in the stationary vehicle setup. This has a considerable effect resulting in lower levels of accumulated water in the AIS. The test case presented in figure 4.8 (d) is most similar to the previously presented setup but produces different results.
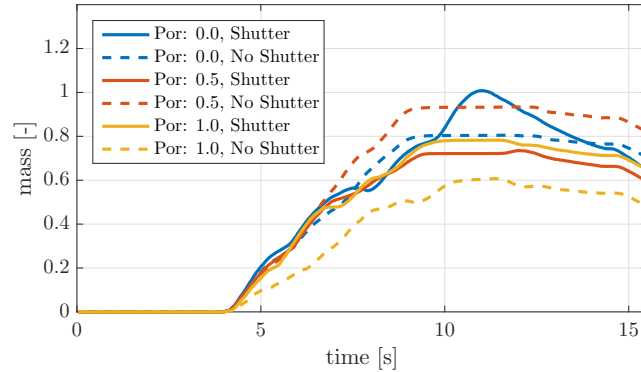

Figure 4.9: *Accumulated mass of water in the AIS measured through a plane in the intake duct. Both the upper shutter and level of porosity of the radiator package have considerable effect on the amount of water entering the AIS. The results have been normalized by the final mass of water in the AIS taken from the VOF simulation.*

4.3   SPH vs Real driving

The suspension model implemented in PreonLab was evaluated by replicating the driving conditions during physical tests at HPG. The two setups were as identical as possible, including the suspension parameters, geometry of the vehicle and channel together with the trajectory. The extracted suspension data from the real tests and PreonLab are presented in this section together with photos of the flow fields. Both front and rear axle data are presented together with the logged vehicle speeds. The vertical black dashed lines in the graphs indicate the interval in which both front and rear wheels are on the flat part of the channel, with full depth. A positive deflection in the suspension equals an extension while a negative equals a compression.

4.3.1   6 km/h - Driving through the middle of the channel

In figure 4.10 (a)-(c) the results from the first experiment and simulation are presented. The same overall behaviour is observed for all four suspension signals. Once the car body hits the water an extension of 2 cm is observed, for both front and rear axles. This happens at the same time front and rear. The extensions are constant over the flat channel section and decreases once the vehicles starts leaving the channels. A compression of the front axles can be observed during the last 5 seconds. This can be explained by the additional weight of water still on top of the panels present under the engine bay. The same phenomena was observed in section 4.2.2, most evident in figure 4.7 (b). The phenomena is greater in the real test compared to PreonLab.

(a) *Front axle*

(b) *Rear axle*

(c) *Vehicle speed*
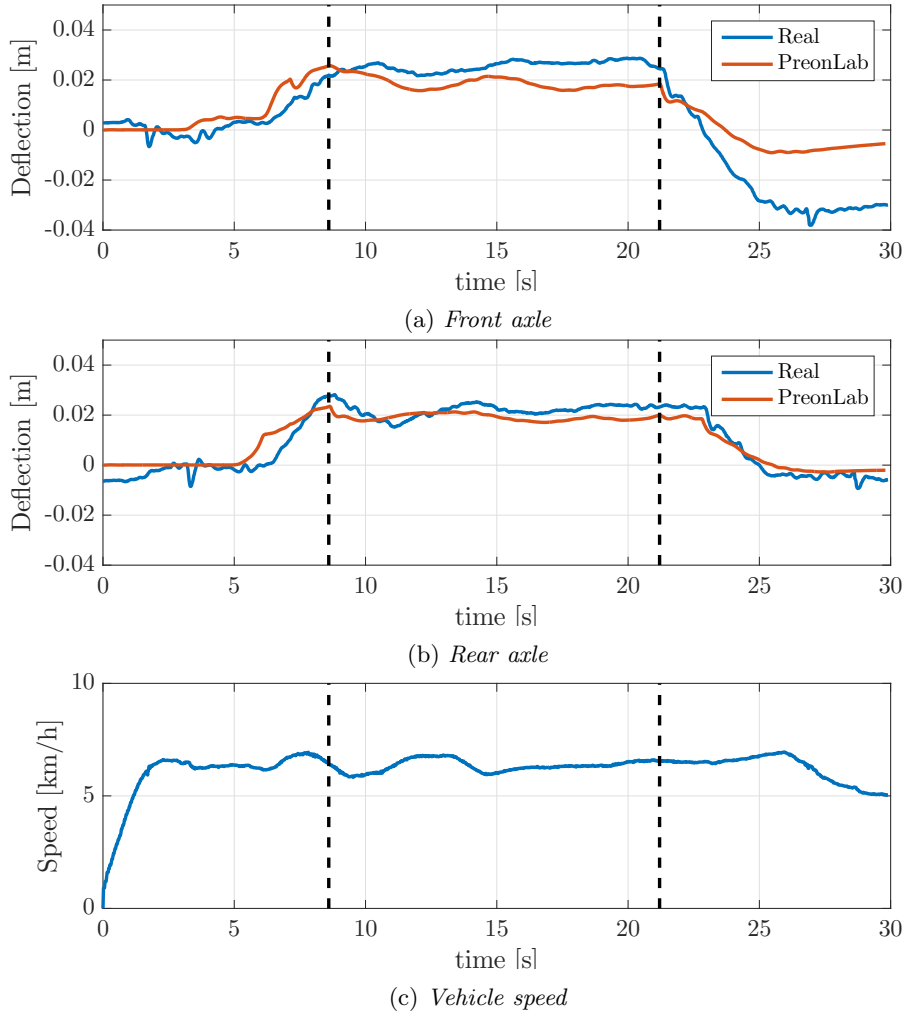
Figure 4.10: *Front and rear axle deflections from the first test setup. The data from the experiment and the simulation show a similar behaviour. There is an under prediction in the compression of the front axle in PreonLab during the last 5 seconds. The compression can be explained by the water trapped in the engine bay pushing the car down.*
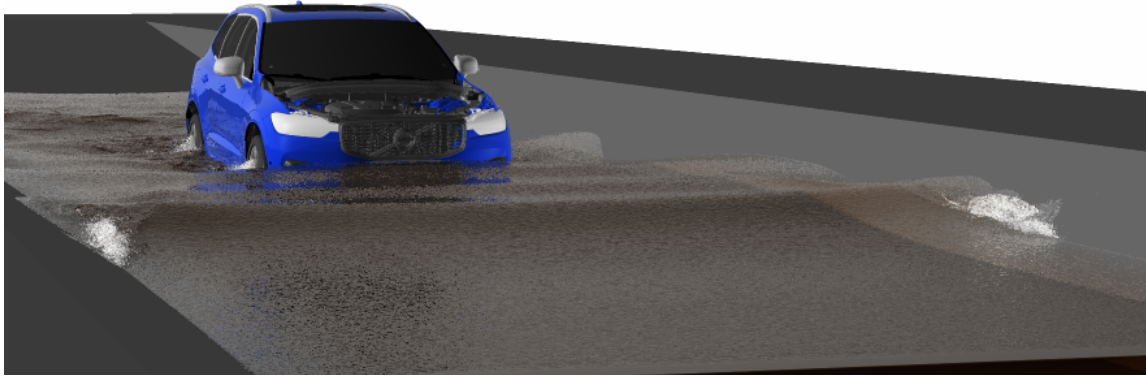
(a) *PreonLab*

(b) *HPG*

Figure 4.11: *Test 1 - 6 km/h. 14 s*

Observing the two images presented in figure 4.11 the two free surfaces can be seen. In (a) the simulated case of the first test is shown, while the physical test is shown in (b). Both figures are taken 14 seconds into the events. The bow waterline appears on the same height in both images. The number plates are partially submerged. In front of the vehicles, three distinct waves can be seen in both images. The foremost one is the most prominent, where a collapse on the sides near to the sloped walls can be observed. The lengths of the upward propagations are difficult to determine from the images, but seem to be similar. No breakups and splashing can be observed near the vehicles. The wheels and especially the spokes seem to create some splashing effect, but the behaviour is very mild.

4.3.2 12 km/h - Driving through the middle of the channel

In figure 4.12 (a)-(c) the results from the second experiment and simulation are presented together with the logged vehicle speed. Looking at figure 4.12 (a) the initial impact with the water on the vehicle bodies are seen by an extension of the front suspensions at approximately 3.5 seconds. Unlike the first test the front axle now extends earlier than the rear. This event occurs at the same time in both the experiment and the simulation. A somewhat larger extension, creating an offset between the two signals, is seen in the real test, which is later amplified until both sets of wheels are fully on the flat test section of the channel. This difference of roughly 2 cm is continuous until the end of the flat channel section. Once the vehicle starts leaving the channel the difference between the two signals is decreased until a similar behaviour is reached. The rear axle deflection has a more similar behaviour comparing the two cases. A larger extension during the second half of the flat channel is observed for the real test. The difference is constant until the vehicles start leaving the channel. The gradual extension during the first half of the flat channel, seen both the front and rear, can be explained by the continuous build-up of the external wave pattern. The target speed is reached by the time both sets of wheels are on the flat part of the channel. A slight increase in the speed is observed during the flat part.

(a) *Front axle*

(b) *Rear axle*

(c) *Vehicle speed*
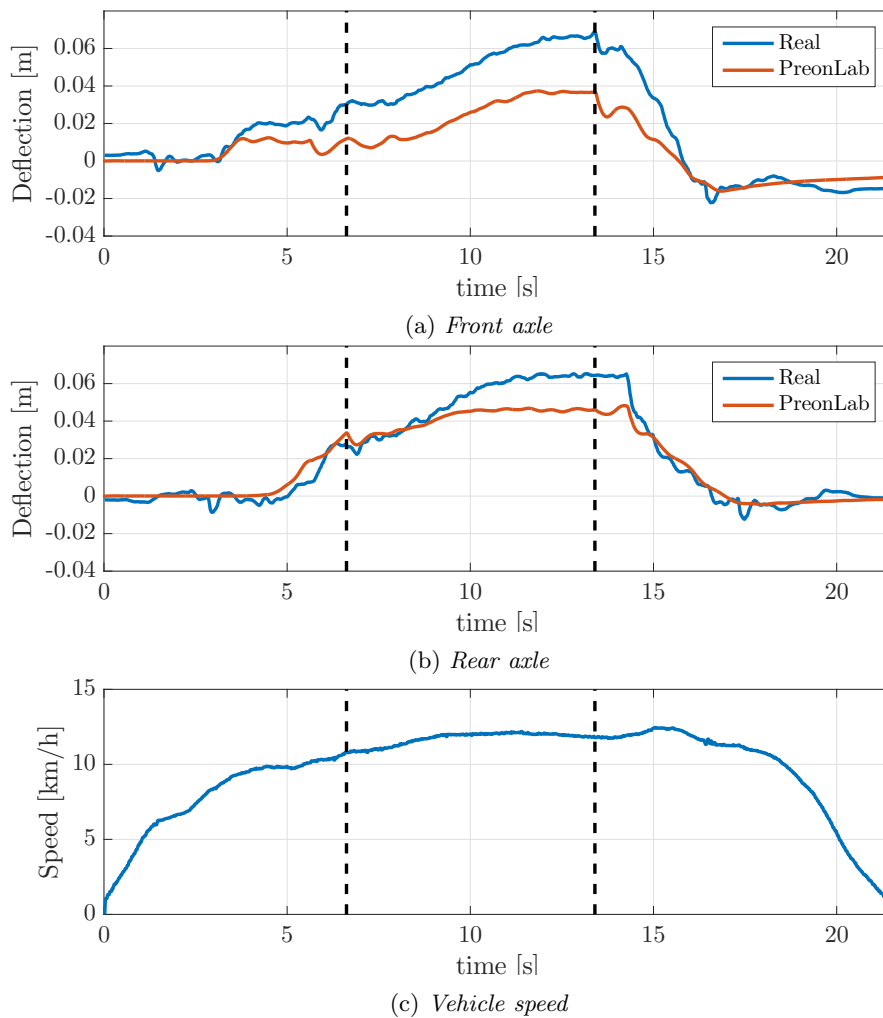
Figure 4.12: *Front and rear axle deflections from the second test setup. The behaviour of the rear axle is captured well in PreonLab except during the second half of the flat part of the channel. The front axle deflection is underpredicted throughout the entire event.*
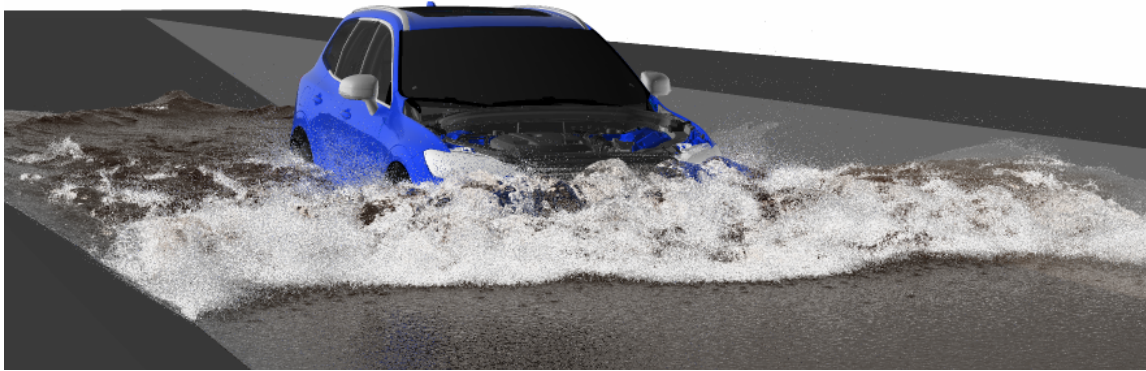
(a) *PreonLab*

(b) *HPG*

Figure 4.13: *Test 2 - 12 km/h. 11 s*

In figure 4.13 the comparison of the free surfaces from the second test are presented. The images are taken 11 seconds into the events. Large bow wave formations can be observed in both images. The waterline goes higher in (a) comparing to (b). This agrees well with the observed behaviour of the front suspension presented in figure 4.12 (a). By lowering the front, the waterline will rise due to the static difference between the vehicle and the undisturbed surface. This will also allow less water to be transported away, under the vehicle, accumulating a larger volume of water in the bow area. The upstream propagation is limited due to the high Froude number and seems to follow the same behaviour. This also applies for the waterline following the vehicle sides.

4.3.3   12 km/h - Driving next to the left edge of the channel

During the third test, driving next to the left sloped wall, a similar behaviour compared to the second test is observed. The results are presented in figure 4.14 (a)-(c). In this test the individual suspension data for each wheel are presented rather than front and rear averages. The front axles are extended earlier than the rear. By the time the front wheels hits the flat part of the channel a rapid extension of roughly 2 cm is observed. This behaviour is not seen in PreonLab. As the speed increases over the flat channel bed the front wheels extend more continuously. The front left wheel extends more than the right, which is expected due to the additional build-up of the wave closer to the sloped wall. The difference, right to left, stays constant at 1 cm during the event. The rear wheels extend equally and the behaviour is captured well by PreonLab. As in the previous tests, there is a final compression of the front wheels while the engine bay is drained.

(a) *Front Axle*


(b) *Rear Axle*

(c) *Vehicle speed*
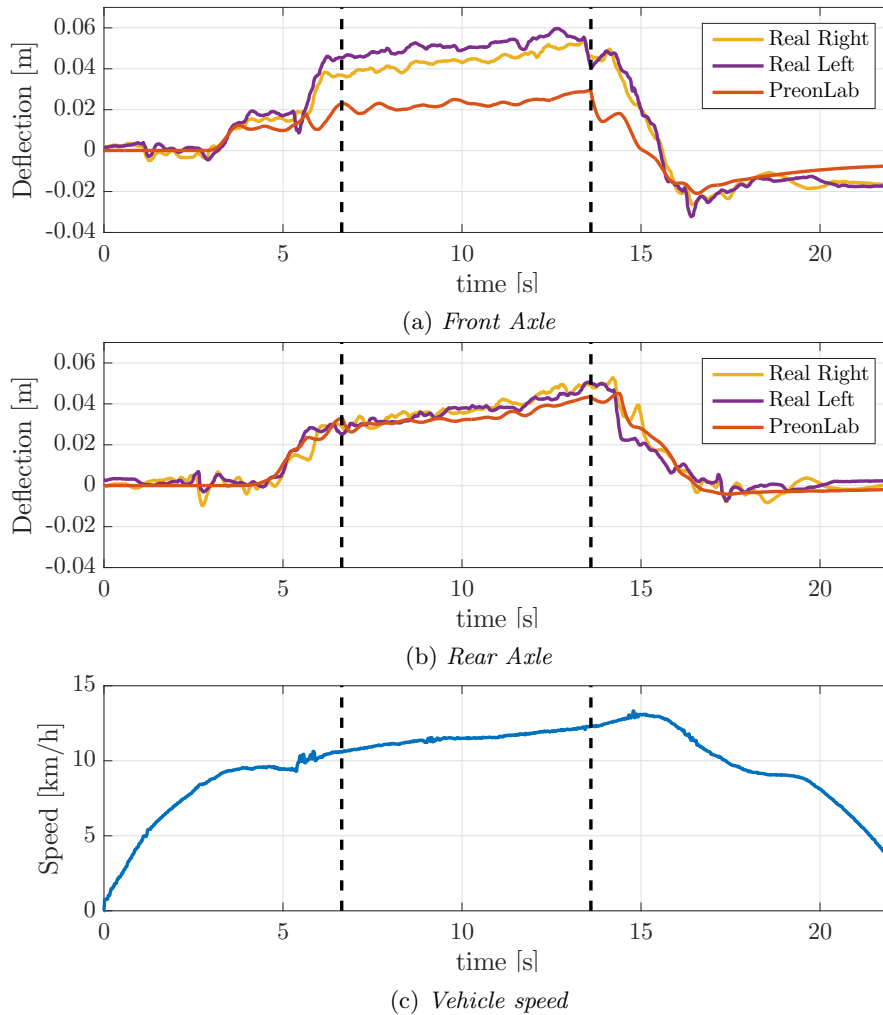
Figure 4.14: *Front and rear wheels deflections from the third test setup. The behaviour of the rear wheels compare good with the rear axle in PreonLab. The front axle is however underpredicted during the whole flat part of the channel. The front left wheel extends 1 cm more than the right.*

4.3.4 Static buoyancy test

In table 4.3 the results for the front and rear axle deflection standing still in the channel are presented. As can be seen, the deflection of the front and rear axle are almost identical in PreonLab while larger differences can be seen in the physical test. This results reminds more of the first test, running at 6 km/h, rather than the later. The static buoyancy, more important at low or no speed seems to be captured reasonably well.

Table 4.3: *Front and rear axle deflection for the experiment and simulation.*

	Front Axle [m]	Rear Axle [m]
Real	0.016	0.029
PreonLab	0.018	0.020

4.3.5 Simulation run times

I table 4.3 the simulation run times for the three dynamic tests are presented. As can be seen, the same number of cores were used for all three simulations. Still, the run time of the third simulation is about 12 % greater than the second despite having the same setup in terms of domain size and vehicle speed. The average number of particles is however 22 million more and the physical simulation time was 0.7 seconds longer.

By reducing the vehicle speed, as in the first test, the simulation run time is increased. There are two reasons for this. The first one is that the physical simulation event is longer compared to the second and third tests. The second reason is that the computational domain had to be extended in front of the vehicle due to the rapid upstream propagating wave. Hence, more particles are present during this simulation.

Table 4.4: *Run times for the three dynamic simulations with the purpose of replicating the physical tests at HPG.*

	Test 1	Test 2	Test 3
Cores [-]	2184	2184	2184
Simulation time [CPUh]	118300	71526	80080
No. of Particles (averaged)	267 000 000	213 000 000	236 000 000
Simulated physical time [s]	29.8	21.4	22.1

5 Discussion

In the following chapter a discussion is given focusing on some of the aspects covered in this thesis. Initially, the use of FVM and SPH are compared and features of both are presented.

5.1 FVM vs SPH

A dilemma can be concluded affecting the comparative value of using the different frames of references in this work. A stationary vehicle setup like the one used in FVM cannot be replicated in real life, hence a correlation of the measured forces is not possible and no conclusion can be drawn regarding whether SPH or VOF predicts forces more accurately. Concurrently, a FVM setup is difficult to achieve with reasonable resources with the purpose of replicate a moving vehicle setup.

Khapane et al. [7] has developed a FVM method employing an overset mesh [20] approach to account for the movement of the vehicle body. The complexity and increase in computational cost was used as arguments for not using rigid body motion of the rims and tires. In their study, it was concluded that the model was suitable at low and medium vehicle speeds where each modelled phase constituted a large structure, with a relatively small contact area. If a large number of breakups occur a smaller mesh size should be used to capture the flow accurately. Khapane et al. describe and have faced the same issues that have been seen here. Comparing the two initial impacts of the VOF and SPH simulations conducted using the stationary vehicle setup in this study, it can be seen that this is the case (figure 5.1). In (b), where the free surface of the SPH simulation is presented, a large number of small breakups are present along the bow formation. The used FVM mesh in (a) is not sufficiently fine to capture all the structures emerging in that particular area. The same conclusions can be drawn looking at figure 5.2, where a cut plane ($y=0$) is presented showing the volume fraction of water. Close to the vehicle body the flow is captures well, showing a sharp interface. However further away, the solution is smeared out. In this sense, SPH has an advantage in its framework. At the same time one needs to decide which regions of the flow that are interesting to resolve and which are not. As was mentioned, FVM is suitable at lower vehicles speed with distinct phase separations. If going at higher speed, which then usually corresponds to traversing through more shallow water, resulting in higher Froude and Weber numbers, breakups become increasingly important and more restrictions are set on the timestep and mesh refinements. If a certain droplet size is to be resolved, fulfilling the same CFL condition, SPH should be able to have a timestep larger than three times that of VOF, given that the spacing in SPH can be considered as individual droplets and a mesh size one third of the droplet diameter in VOF is used [20].

Moreover, a one way coupling approach was used by Khapane et al., where the forces acting on the vehicle were not taken into account while moving the vehicle through the channel. An adaptive vehicle speed was however used in a similar fashion as in this work to approximately account for the external forces. Again, this is due to the computational cost associated with these actions. The implemented suspension model in PreonLab is however a two-way coupling approach which improves the modelling, without adding a considerable computational cost.

A two-way coupling to account for the vehicle speed is reasonable and should be possible to implement in PreonLab. By doing this, the simulation is not dependent on physically acquired data, which most likely will be problem dependent. By doing a coupling using the measured forces as inputs into Python, where a simplified vehicle model can be implemented to adjust the vehicle speed at every timestep, these phenomena should be able to be accounted for.

5.1.1 Differences in the geometries

Focusing on this work only, differences in the geometry between SPH and VOF can be discussed. As the gap boundary method was used in SPH a thickening effect of all surfaces was achieved. This could be one of the reasons there are differences in the external flow fields, even though this effect might be small or even negligible. This problem becomes less important for smaller particles. For future work, the more expensive no-gap boundary method should be tested in order to investigate its influence on the exterior flow.

| (a) VOF | (b) SPH |

Figure 5.1: *Initial impact, at 2 seconds of physical simulation time, using the stationary vehicle setup. As can be seen in (b) a larger quantity of small breakups occur due to the bow wave formation. The surface is colored by the position in z. A large number of single particles are sprayed up and outwards during the initial impact in SPH. This suggest that there are some numerical instabilities in the solver.*


Volume Fraction Water [-]

| 0 | 0.5 | 1 |

Figure 5.2: *Volume fraction of water seen through a cut plane (y=0) showing the bow wave formation using VOF at 2 seconds of physical simulation time. Near the car body the flow is resolved to a higher level than further away resulting in smearing effect of the finer structures.*

5.1.2 Differences in the calculated surface forces

It's interesting to look at the observed forces acting on the panels in section 4.1.3. The graphs suggest that SPH overpredicts forces relative VOF. In some cases, the SPH solutions converges to values close to those seen in VOF, while in others, convergence to something completely different is seen. One explanation for this could be that the flow field is different and therefore the real forces differ. A more robust way of determining the derived forces would be to conduct isolated and controlled simulations on a smaller scale comparing the different methods. This should also be compared to physical testing, as the validity of the VOF results are uncertain. In a design perspective an overprediction of the calculated forces lead to a more conservative design, but might also result in heavier and more expensive components.

5.1.3 Simulation run times

Comparing SPH with VOF, the former has many advantages in terms of time consumption. In both methods, a geometry import is necessary. Compared to StarCCM+, where a full volume mesh is needed, PreonLab has the big advantage that the existing mesh taken from the actual CAD can be used without further processing. If one wants to configure the tessellation, making it coarser or finer, this can be done in an intermediate step using ANSA, for instance. Volume meshing takes time and many iterations may be needed in order to fix bad cells.

In terms of simulation run time, comparing with the particle spacings used in this work, SPH is much faster and no issues regarding diverging solutions have occurred. The simulation run time seem to have many variables affecting it. As was seen in table 4.1, comparing VOF and SPH, the simulation time decreased almost linearly with an increased particle spacing for a fixed number of cores. In table 4.2, the domain size was investigated and the number of cores differed between the simulations. By using 2160 cores instead of 1232 and at the same time reducing the number of simulated particles the total simulation time increased. The reason for this is unknown. For this particular setup it was most efficient, in terms of core hours, to run on 984 cores.

Most interesting is to compare the VOF results with the ones presented in table 4.4, where the suspension model was implemented. This setup is the most realistic in terms of vehicle speed, vehicle movement and buoyancy effects. For the second test running at 12 km/h 71526 core hours were used, but the simulation was performed using 2184 cores, which seems to be less effective than running on fewer. The VOF simulation on the other hand took 151124 core hours on 1232 cores.

Using the information gathered from the different phases in this work, an optimal setup, in regards to the information known can be developed in terms of simulation run time. The wake resolvement can be reduced, which can almost cut the total simulation time in half, compared to the time taken using a 22 m long domain. The domain in front of the vehicle can also be reduced. Using the information from figure 4.5 the domain in front of the vehicle can be cut by another 5.5 m, thus removing roughly a fourth of the initial particle number. Doing these modifications together with using an optimal number of cores, the simulation time should be possible to reduce to under 20000 core hours, given that the finest particle spacing is used. This reasoning is only valid at the highest tested vehicle speed. For lower speeds, the physical event will be longer, the wave upstream is more developed and the influence of the wake resolvement is yet unknown.

5.2 Features of SPH

Putting FVM aside, model specific features of SPH are presented below.

5.2.1 Suspension model

Looking at the suspension model, this function seems to work quite accurately. A theory to explain the underpredictions of the results in PreonLab is related to the influence of the air suspension system present in the vehicle used in the physical tests. This system actively tries to adjust the ride height to be equal front and rear. If the system kicks in and adjust the ride height, the vehicle will settle in a new steady position. The rapid extension visible of the front wheels during the third test, in section 4.3.3, is an indication that the system tries to do some sort of correction. Looking at figure 4.14 (b), the rear suspension extends further than the front at approximately 6 seconds, triggering the system to extend the front additionally. Assuming this is the case, the behaviour of the simulation agrees well with the experiment. Adopting the same assumption in the second test, good agreement is found here as well. A system like this, actively trying to correct the ride height, can currently not be implemented in PreonLab. If the suspension model function is to be used in a new

method to simulate wading, this has to be specified in the requirements. As a part of future work, similar tests at HPG should be performed where the active air suspension system is either monitored or disabled.

One flaw in the current suspension model in PreonLab has been found. As the wheel base is completely scripted to follow the channel floor the wheels cannot lift from the ground. If the vehicle is travelling at a sufficiently high speed the wheels and car body will initially skid on the water. If the suspension model is implemented in a case like this, the car body will be pulled downwards once the suspension has been extended fully. This will have an immense effect on the validity of the simulation.

5.2.2 Simulated particle sizes

The size of the particles seem to have a small influence on the exterior water behaviour. If for instance waterlines are of interest, a larger particle size could be used. Larger particles do however dampen smaller structures and breakups, which might be of interest if splashing and dry/wet areas on the vehicle are of interest. If on the other hand, water ingress is studied, the spacing becomes increasingly important as the result might be affected by particles not flowing freely through tight gaps in the body structure. As was seen in section 4.1.2, the amount of water entering the AIS is influenced by the particle spacing. What has not been investigated in this study is how the different boundary handling methods affect flow through tight areas. By adopting the no-gap model for the boundary particles, a larger particle size might be possible to use while acquiring the same results. The no-gap model does however use a different kernel function, introducing more boundary particles, which might actually increase the total number of simulated particles and hence the computational cost.

5.2.3 Influence of the domain size

As discussed above, cutting the rear of the domain does not affect the wave pattern significantly. Moreover, the extracted panel forces stays unaffected as well. This indicates that there is little to no upstream wake propagation. What the outcome will be if the same domain sizes are simulated at a lower vehicle speed is not known. At a smaller Froude number this domain size reduction might have a larger effect. This should further be investigated as the simulation run time can be reduced dramatically. The same thing can be applied to the upstream part of the domain. Going at speed creating a supercritical Froude number a smaller domain upstream of the vehicle can be applied. In terms of subcritical Froude numbers, either a large body upstream is included in the computational domain initially or the domain is allowed to extend away from the vehicle as the simulation progresses. By doing the latter, one can ensure having a domain as small as possible at all times.

5.2.4 Radiator modelling

By changing the porosity of the radiator package, different flow fields were acquired, allowing water to be drained from the area in front of the vehicle. At this time no reliable model is available and physical testing is needed in order to tune the system to behave in a similar fashion as a real radiator system would. Which approach to choose, modelling the system or not, is yet to be determined. One alternative is to put more effort into finding proper constants to model the package, making the physics and the flow field more realistic. The other alternative is to keep the package completely shut, forcing more water to accumulate in the region of interest. The latter alternative makes the requirements harder to fulfil and hence the system more robust to actual water ingress in the AIS.

5.3 Validity of using a wading channel

One can discuss how realistic driving through the physical channel actually is and how it compares to driving in open water. By looking at the results, especially in the stationary vehicle setup, it seems like the side walls hinder water from moving out to the sides, trapping it upstream of the vehicle. If this is the case, the waterline on the front part of the vehicle will be higher than what it would be during open water driving. Once again, this should make for a more difficult fulfilment of the requirements set by the specification of the vehicle, resulting in a more robust design.

6 Conclusions

In this thesis the use of SPH and more specifically PreonLab is investigated in order to determine its usefulness as a complement or substitute to VOF when conducting wading simulations at VCC. The thesis is divided into three parts. The first one focuses on comparing SPH and VOF in terms of wave propagation, exerted forces on panels, water intake and simulation run time. A setup, using a stationary vehicle approach is used, as this is what the previous method using FVM is adopting. Both methods seem to predict a similar behaviour of the flow, while in SPH, larger forces on exterior vehicle panels are predicted. Three different particle spacings are employed in SPH. Similar results are acquired, using the different spacings, but a trend of smaller forces are observed with a decreasing particle spacing. The validity of the results are difficult to determine, both in VOF and SPH, as a stationary vehicle setup is not feasible for physical testing. Therefore, in order to determine if VOF or SPH predicts the forces more accurately, isolated tests on a smaller scale should be conducted.

The computational domain size used in SPH is investigated and the requirements on the dimensions is highly dependent on the test setup in terms of the vehicle speed and most likely the wading depth. The domain size should be adjusted per case in order to minimize the computation cost.

A setup, similar to one used in physical testing, is implemented in PreonLab where the free surface and suspension dynamics due to buoyancy effects are investigated. The measured suspension data correlates well with simulations and most phenomena seem to be captured. An active suspension system present in the real vehicle is likely to be the main cause of an underprediction of the dynamics in PreonLab. This needs to be investigated further.

The advantages of SPH, e.g. not being reliable on a computational mesh and shorter simulation times, are shown in this report. A baseline for further development is presented, where multiple recommendations are given to make an even more robust model.

References

[1] *Road transport: Reducing CO2 emissions from vehicles.* EU. 2019. URL: https://ec.europa.eu/clima/policies/transport/vehicles_en (visited on 05/30/2019).

[2] *The Paris Agreement.* UNFCCC. 2017. URL: https://unfccc.int/process-and-meetings/the-paris-agreement/d2hhdC1pcy (visited on 05/30/2019).

[3] *About Volvo Cars.* Volvo Car Corporation. 2019. URL: https://group.volvocars.com/company (visited on 05/30/2019).

[4] J. Monaghan. Smoothed Particle Hydrodynamics. *Annu. Rev. Astron. Astrophys* **30** (1992), 543–574.

[5] C. T. Crowe et al. *Multiphase flows with droplets and particles.* Taylor and Francis Group, 2012. ISBN: 13: 978-1-4398-4051-1.

[6] S. Sasic. "Multiphase flows, Lecture 2 - Equation of motion of a single particle, forces on individual particles". University Lecture. 2018.

[7] P. Khapane, V. Chavan, and U. Ganeshwade. Water Ingress Analysis and Splash Protection Evaluation for Vehicle Wading using Non-Classical CFD Simulation. *SAE Int. J. Passeng. Cars - Mech. Syst.* **10(1)** (2017), 183–194.

[8] S. Sasic. "Multiphase flows, Lecture 6 - Multiscale modelling of multiphase flows: Direct Numerical Simulations (DNS) of multiphase flows". University Lecture. 2018.

[9] A. M. Tartakovsky and A. Panchenka. Pairwise Force Smoothed Particle Hydrodynamics model for multiphase flows: Surface tension and contact dynamics. *Journal of Computational Physics* **305** (2016), 1119–1146.

[10] *Theory Preon Solver. Momentum Equation.* Version 3.2. Fifty2 Technology GmbH, 2018.

[11] J. P. Morris, P. J. Fox, and Y. Zhu. Modelling Low Reynolds Number Incompressible Flows Using SPH. *Journal of Computational Physics* **136** (1997), 214–226.

[12] S. Shao and E. Y. Lo. Incompressible SPH method for simulating Newtonian and non-Newtonian flows with a free surface. *Adv Water Resour* **26** (2003), 787–800.

[13] A. Rafiee and K. P. Thiagarajan. An SPH projection method for simulating fluid-hypoelastic structure interaction. *Comput Methods Appl Mech Eng* **198** (2009), 2785–2795.

[14] A. Ferrari et al. A new 3D parallel SPH scheme for free surface flows. *Computers and fluids* **38** (2008), 1203–1217.

[15] J. Monaghan and J. Kajtar. SPH particle boundary forces for arbitrary boundaries. *Computer Physics Communications* **180** (2009), 1811–1820.

[16] A. Colagrossi and M. Landrini. Numerical simulation of interfacial flows by smoothed particle hydrodynamics. *Journal of Computational Physics* **191** (2003), 448–475.

[17] C. Ulrich, M. Leonardi, and T. Rung. Multi-physics SPH simulation of complex marine-engineering hydrodynamic problems. *Ocean Engineering* **64** (2013), 109–121.

[18] *PreonLab Manual. Timestep computation.* Version 3.2. Fifty2 Technology GmbH, 2018.

[19] F. M. White. *Fluid Mechanics - Seventh edition in SI units.* McGraw-Hill Education, 2011. ISBN: 978-007-131121-2.

[20] *STAR-CCM+ User Manual.* 13th ed. Siemens.